Galaxy formation in the reionization epoch as hinted by Wide Field Camera 3 observations of the Hubble Ultra Deep Field

Hao-Jing Yan[1], Rogier A. Windhorst[2], Nimish P. Hathi[3], Seth H. Cohen[2], Russell E. Ryan[4], Robert W. O'Connell[5] and Patrick J. McCarthy[6]

[1] Center for Cosmology and AstroParticle Physics, The Ohio State University, 191 West Woodruff Avenue, Columbus, OH 43210, USA; *yanhaojing@gmail.com*
[2] School of Earth and Space Exploration, Arizona State University, Tempe, AZ 85287, USA;
[3] Department of Physics & Astronomy, University of California, Riverside, CA 92521, USA;
[4] Department of Physics, University of California, One Shields Avenue, Davis, CA 95616, USA;
[5] Astronomy Department, University of Virginia, P.O. Box 3818, Charlottesville, VA 22903, USA;
[6] Observatories of the Carnegie Institution of Washington, 813 Santa Barbara Street, Pasadena, CA 91101, USA

Abstract We present a large sample of candidate galaxies at $z \approx 7 - 10$, selected in the Hubble Ultra Deep Field using the new observations of the Wide Field Camera 3 that was recently installed on the Hubble Space Telescope. Our sample is composed of 20 z_{850}-dropouts (four new discoveries), 15 Y_{105}-dropouts (nine new discoveries) and 20 J_{125}-dropouts (all new discoveries). The surface densities of the z_{850}-dropouts are close to what was predicted by earlier studies, however, those of the Y_{105}- and J_{125}-dropouts are quite unexpected. While no Y_{105}- or J_{125}-dropouts have been found at $AB \leq 28.0$ mag, their surface densities seem to increase sharply at fainter levels. While some of these candidates seem to be close to foreground galaxies and thus could possibly be gravitationally lensed, the overall surface densities after excluding such cases are still much higher than what would be expected if the luminosity function does not evolve from $z \sim 7$ to 10. Motivated by such steep increases, we tentatively propose a set of Schechter function parameters to describe the luminosity functions at $z \approx 8$ and 10. As compared to their counterpart at $z \approx 7$, here L^* decreases by a factor of ~ 6.5 and Φ^* increases by a factor of 17–90. Although such parameters are not yet demanded by the existing observations, they are allowed and seem to agree with the data better than other alternatives. If these luminosity functions are still valid beyond our current detection limit, this would imply a sudden emergence of a large number of low-luminosity galaxies when looking back in time to $z \approx 10$, which, while seemingly exotic, would naturally fit in the picture of the cosmic hydrogen reionization. These early galaxies could easily account for the ionizing photon budget required by the reionization, and they would imply that the global star formation rate density might start from a very high value at $z \approx 10$, rapidly reach the minimum at $z \approx 7$, and start to rise again towards $z \approx 6$. In this scenario, the majority of the stellar mass that the universe assembled through the reionization epoch seems still undetected by current observations at $z \approx 6$.

Key words: cosmology: observations — cosmology: early universe — galaxies: evolution — galaxies: luminosity function, mass function — infrared: galaxies

1 INTRODUCTION

An important subject in cosmology is the hydrogen reionization of the universe. The detections of complete Gunn-Peterson troughs (Gunn & Peterson 1965) in the spectra of a few $z > 6$ QSOs (see Fan et al. 2006) from the Sloan Digital Sky Survey indicate that the reionization must have ended at around $z \approx 6$, while the recent measurement of Thomson scattering optical depth from the seven-year Wilkinson Microwave Anisotropy Probe (WMAP) data shows that the reionization most likely began at $z = 10.4 \pm 1.2$ if assuming an instantaneous reionization history (Komatsu et al. 2010). An important and yet controversial question is the sources of reionization. It is clear that the QSO population can only produce a small fraction of the necessary ionizing photons at $z \approx 6$ (e.g., Fan et al. 2002), which leaves star-forming galaxies as the most obvious alternative, although the measurement of the star-formation rate density (and hence the ionizing photon budget) is still uncertain (e.g., Stanway et al. 2003; Bouwens et al. 2003; Giavalisco et al. 2004b; Bunker et al. 2004; Yan & Windhorst 2004b). Yan & Windhorst (2004a; hereafter YW04a) pointed out that star-forming galaxies could account for the entire ionizing photon budget at $z \approx 6$ as long as their luminosity function (LF) has a steep faint-end slope, $\alpha < -1.6$. Using the Hubble Ultra Deep Field (HUDF; Beckwith et al. 2006) data obtained by the Advanced Camera for Surveys (ACS), Yan & Windhorst (2004b; hereafter YW04b) have found a large number of i_{775}-dropouts, which are candidate galaxies at $z \approx 6$, and obtained their LF that indeed has $\alpha \lesssim -1.8$. Such a very steep slope was later confirmed by Bouwens et al. (2006) using a larger i_{775}-dropout sample collected in the HUDF, the HUDF parallel fields and the two fields of the Great Observatories Origins Deep Survey (GOODS; Giavalisco et al. 2004a). Bouwens et al. (2007; hereafter B07) further compared the LF at $z \approx 4$, 5 and 6, and suggested that the LF has a strong luminosity evolution over this period in that M^* is ~ 0.7 mag fainter at $z \approx 6$ than at $z \approx 4$. On the other hand, they found that the LF does not change much in α. Since star-forming galaxies seem to be capable of keeping the universe ionized at $z \approx 6$, it is natural to expect that star-forming galaxies are also capable of producing sufficient ionizing photons at earlier epochs to make the reionization happen, and therefore we should expect that they must exist in significant numbers extending well into the reionization epoch.

Along a different line of study, it has also been concluded that the universe must have started actively forming stars long before $z \approx 6$. Using the GOODS *Spitzer* Infrared Array Camera (IRAC) data in the HUDF region, Yan et al. (2005) have detected the restframe optical fluxes from three $z \approx 6$ and eleven $z \approx 5$ galaxies in the 3.6 and 4.5 μm channels, and found that these are rather mature systems with stellar masses on the order of $\sim 10^{10} M_\odot$ and ages on the order of a few hundred Myr (see also Eyles et al. 2005). This strongly suggests that such high-mass galaxies must have started forming their stars at $z > 7$ and likely earlier. Yan et al. (2006) further investigated this problem using a much larger sample in the entire GOODS field, and reinforced this conclusion (see also Eyles et al. 2007; Stark et al. 2007). Therefore, one should indeed expect a significant number of galaxies at $z \gtrsim 7$.

To search for galaxies at $z \gtrsim 7$, we have to carry out surveys in the near-IR regime, because the line-of-sight neutral hydrogen absorption effectively leads to light extinction from such sources that is emitted below 1 μm in the observer's frame. In fact, we rely on this effect to identify such galaxies. The first candidate of this kind was reported by Dickinson et al. (2000) using the data obtained by the Near Infrared Camera and Multi-Object Spectrometer (NICMOS) No. 3 (NIC3) in the Hubble Deep Field, although now we have convincing evidence that it is likely a red galaxy at lower redshift, similar to those "IRAC-selected Extremely Red Objects" (IERO; Yan et al. 2004). Using the two broad-band data sets taken by NIC3 in the HUDF (Thompson et al. 2005), YW04b identified three objects that are missing from the ACS images. Subsequent analysis using the Spitzer IRAC data suggest that two of them are red galaxies at $z \approx 2$–3 without much on-going star formation (Yan et al. 2004; but also see Mobasher et al. 2005 and Chary et al. 2007), while the third one (ID No.3) is less conclusive because it is blended with other sources in the IRAC image and thus its photometry

is uncertain. Bouwens et al. (2004) used the same data set, pushed to a fainter limit, and found a few additional candidates. Bouwens et al. (2005) further included all available deep NIC3 imaging data and extended their search to $z \approx 10$, although no conclusive answer was obtained. Using these results, Bouwens et al. (2008; hereafter B08) derived constraints on the UV LF of galaxies at $z \approx 7$–10, and argued that the LF evolves strongly and continues the dimming trend in L^* (as proposed in B06) to higher redshifts. As a result, the number density of galaxies, and hence the UV luminosity density in the earlier universe, should be significantly lower than at a later time.

Meanwhile, the search for gravitationally lensed galaxies around foreground galaxy clusters has resulted in some remarkable success. Kneib et al. (2004) first discovered such an object that is likely at $z > 6$. While no precise redshift was obtained, extensive optical and IR observations suggest that it is at $z \approx 7$. Bradley et al. (2008) reported a very bright, highly probable candidate at $z \approx 7.6$. Zheng et al. (2009) reported three new $z \approx 7$ candidates from the same campaign. Richard et al. (2008) have found 12 candidates at similar redshifts. These results, however, still do not allow us to put a strong constraint on the number density of galaxies at these redshifts, although they indeed prove that very high-redshift galaxies, much fainter than our current detection limits (should there be no lensing magnification), do exist. There is also some other evidence from the search for Lyα emitters around foreground clusters that supports the similar conclusion (Stark et al. 2007).

While the above results start to give us some meaningful constraints on the faint-end of the LF at $z \gtrsim 7$, there are still only limited constraints on the bright-end where deep wide-field surveys are required. To date, most such surveys have null detection (e.g., Willis et al. 2008; Stanway et al. 2008; Sobral et al. 2009) or are uncertain (e.g. Hickey et al. 2010). One exception that has produced positive detections is the Subaru CCD survey for LAEs at $z = 7.0 \pm 0.1$, which has resulted in the redshift record of $z = 6.96$ (Iye et al. 2006). However, even such LAEs can only constrain the faint population, as the vast majority of them are pure emission-line objects and are not seen in the continuum. Another exception is that of Ouchi et al. (2009), who surveyed ~ 1500 arcmin^2 in two fields which resulted in 22 $z \approx 7$ candidates to $AB \sim 26.0$ mag. Recently, Capak et al. (2009) reported three very bright candidates with $z \approx 7$ at $J \sim 23$ mag, however, their nature is still uncertain.

Nearly all these studies (with the exception of Capak et al. 2009) in the very high-redshift frontier have claimed that their results are consistent with the strong declining evolution of the LF with respect to increasing redshift as suggested by B07 and B08. If this is indeed how the universe behaves, we are facing a dilemma: on one hand, the hydrogen reionization, which most likely has started at $z \approx 10$, requires a large amount of strong UV emitting sources, and the significant stellar mass density measured at $z \approx 6$ also strongly suggests very active star formation activities at $z \gtrsim 8$ and above; on the other hand, the limited number of observations to search for galaxies beyond $z \approx 7$ indicates a strongly declining number density of galaxies at higher redshifts. To reconcile these seemingly conflicted results, a more decisive survey for galaxies at $z \gtrsim 7$ is in demand.

The Wide Field Camera 3 (WFC3) recently installed on *HST* has provided a unique opportunity for the study of the universe at very high redshifts. The IR channel of this camera has a factor of $6.4\times$ larger field-of-view (FOV) and an order of magnitude higher Q.E. compared to NIC3, making it the most powerful tool for detecting galaxies at $z \approx 7$ and beyond. For this reason, the first set of deep data that it took has already inspired four papers to appear at the arXiv preprint service within one week after the data were made public (Bouwens et al. 2010; Oesch et al. 2010; Bunker et al. 2009; McLure et al. 2010). All these new results, however, seem to reiterate that the number density of galaxies rapidly declines when we look further back in time. Here we present our results based on an independent reduction and analysis of these data. Our effort has resulted in more candidate galaxies at $z \gtrsim 7$ than others, and, for the first time, a large sample of highly probable candidate galaxies at $z \approx 10$. We will show that our analysis has led to a completely new, although still tentative, conclusion about the formation and evolution of galaxies in the early universe.

Our paper is organized as follows. We briefly describe the WFC3 IR instrument and its observations of the HUDF in Section 2, and give the details of our data reduction in Section 3. Our photometry and catalog construction are described in Section 4. The candidate selection and the dropout samples are presented in Section 5. We discuss the implications of our results in Section 6, followed by a summary in Section 7. For simplicity, we denote the ACS passbands F435W, F606W, F775W, and F850LP as B_{435}, V_{606}, i_{775}, and z_{850}, respectively, and denote the three WFC3 IR passbands F105W, F125W and F160W as Y_{105}, J_{125} and H_{160}, respectively. All magnitudes quoted are in the AB system. Throughout the paper, we use the following cosmological parameters: $\Omega_M = 0.27$, $\Omega_\Lambda = 0.73$ and $H_0 = 71$ km s^{-1} Mpc^{-1}.

2 WFC3 IR OBSERVATIONS OF THE HUDF

We have used the first epoch of data from the HST Cycle-17 General Observer Program of Illingworth et al. (PID. GO-11563; Bouwens et al. 2010; Oesch et al. 2010), which was designed to do very deep WFC3/IR observations in the three existing, deepest HST fields. Below we briefly describe the instrument and the observations.

The detector of WFC3/IR is an HgCdTe array with 1024×1024 square pixels of 18μm $\times 18\mu$m in size, and is sensitive from 400 to 1700 nm (HST WFC3 Handbook; Kimble et al. 2008). To complement WFC3/UVIS, WFC3/IR is equipped with filters at wavelengths $\gtrsim 800$ nm, and its performance is optimized for wavelengths at $\gtrsim 1000$ nm, where the detector sensitivity reaches its peak. It uses CMOS circuits to make non-destructive readouts in four separate 512×512 quadrants. The effective total area of the array is 1014×1014 pixels, as the outer 5 pixels around the four edges of the detector are blocked from light and are used as "reference pixels," which provide constant-voltage reference values for the readout circuits to help monitor and remove the drift in the electronics. For this reason, WFC3/IR does not suffer from the "pedestal" variations that are common to NICMOS data. While it replaces WFPC2 (and therefore is on-axis), WFC3 still has significant geometric distortion because its focal plane is tilted with respect to the optical axis. The projected IR pixels on the sky are rectangles with scales of $0.121'' \times 0.135''$ and the camera has a total FOV of 4.67 arcmin^2. The camera can be operated in either the imaging mode or the slitless spectroscopy mode.

Program GO-11563 is doing very deep WFC3/IR imaging in the HUDF (Beckwith et al. 2006) and the two HUDF05 fields (Oesch et al. 2007), taking advantage of the extremely deep ACS optical imaging data that already exist. It uses three broad-band filters, namely, Y_{105}, J_{125} and H_{160}. As illustrated in Figure 1, this filter combination offers the capability of selecting galaxies at $z \gtrsim 7$–10 using the dropout technique to detect the Lyman-break signature that occurs at restframe 1216 Å. This program has been allocated 192 orbits: 22 orbits of Y_{105}, 36 orbits of J_{125} and 38 orbits of H_{160} are for the HUDF, while 11 orbits of Y_{105}, 18 orbits of J_{125} and 19 orbits of H_{160} are for each of the HUDF05 fields. The intended depths are ~ 29.0 mag in the HUDF and ~ 28.6 mag in the HUDF05. The observations are packed in visits of four orbits, with each orbit being split into two 1402.9-s exposures operated in the MULTIACCUM mode using the SPARS100 sequence of 15 samplings. A "half-pixel" dithering strategy is used to improve image quality and resolution.

The first epoch of observations was only done in the HUDF, and the data were taken from 2009 August 26 to 2009 September 6. The remaining observations will be executed in year 2010. The obtained data, which include 18 orbits in Y_{105}, 16 orbits in J_{125} and 28 orbits in H_{160}, were made public on 2009 September 9. The observations were oriented to have a similar position angle as the HUDF ACS images, and the field was centered on RA=3$^{\rm h}$32$^{\rm m}$38.5$^{\rm s}$, Dec=$-27°47'0.0''$ (J2000.0). As mentioned in Bouwens et al. (2010) and Oesch et al. (2010), two orbits in Y_{105} were affected by image persistence from earlier exposures in an unrelated program, and these data were excluded from their analysis. Bunker et al. (2009) and McLure et al. (2010) opted to do the same. In fact, two other orbits in H_{160} were also affected by image persistence to the same degree. However, the serious effects are limited to a small region close to the center of the detector. We have decided to
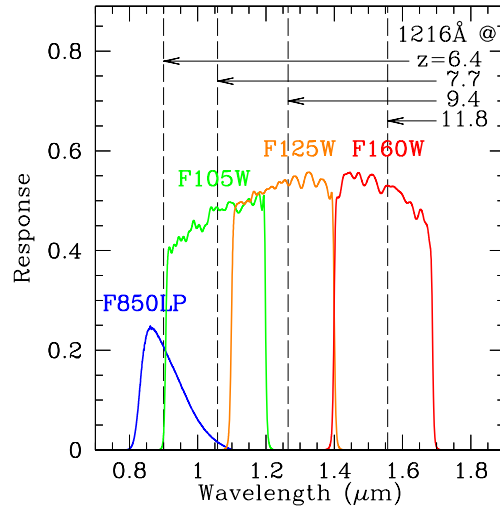
Fig. 1 System response curves of the four major passbands used in this study. Dashed vertical lines indicate the locations of the Lyman-break signature (which occurs at the restframe $\sim 1216\text{Å}$ for galaxies at $z \gtrsim 4$) at various redshifts and demonstrates how galaxies at progressively higher redshifts can be selected as dropouts through successive passbands moving to the redder wavelengths.

include these images in our analysis. As described below, our reduction has successfully masked out the affected pixels, and thus we have taken full advantage of the entire data set. The total effective exposure times are 50505.7, 44894.0, and 78564.5 s in Y_{105}, J_{125} and H_{160}, respectively.

3 DATA REDUCTION

In this section, we provide the details of our data reduction procedure.

3.1 Basic Calibration

The public data released on 2009 September 9 include the raw images and the *HST* pipeline processed images. While the latter ones are the flat-field corrected products, their Data Quality (DQ) extensions have been populated with masks of cosmic rays identified by the pipeline using default parameters that were still preliminary. Therefore, we re-processed the raw images on our own, using the CALWF3 task (Version 1.6, implemented on 2009 April 27) included in the STSDAS package (Version 3.10) and the latest reference files (as of September 9, 2009). Our first-step products from this procedure are the same as those distributed in the public archive, with the exception that the DQ extensions only include the "static mask" that identifies the bad pixels of the detector.

During this step, we noticed that the four quadrants of the processed images had notable offsets at the level of 1%–3%. The inspection of the processed results in the public archive revealed the same problem. This seems to suggest that there are quadrant-dependent bias residuals similar to the so-called "pedestal" in a NICMOS image. However, this was unexpected for the WFC3/IR data, as the reference pixels have been used to remove such drifts (see Sect. 2). It was soon discovered that these offsets were actually caused by a confusion in assigning calibration steps, which has led
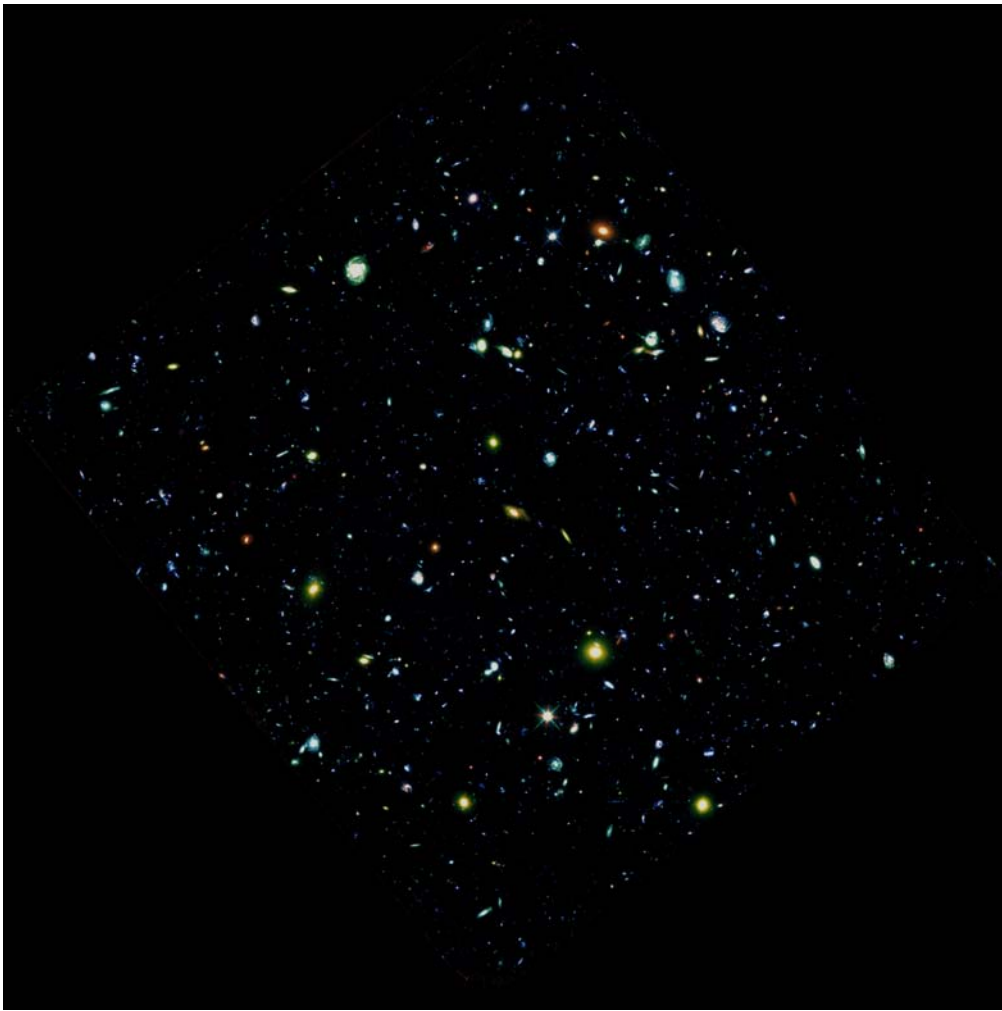
Fig. 2 Color-composite image of the HUDF, created using the weighted-mean of the three-band WFC3/IR mosaics that we made (*red*), the ACS i_{775} (*green*), and the ACS B_{435} (*blue*).

CALWF3 to apply the gain corrections of the four quadrants twice [1]. We manually fixed this problem by applying the appropriate corrections (H. Bushouse, priv. comm.) to the four quadrants. The end result is very satisfactory; the offsets disappear completely [2]. We further inspected the sky-subtracted, median-combined images in each band, and noticed that a small, smooth background gradient was still present at the $\sim 1\%$ level. This gradient was removed by fitting a plane to each individual image; the mean sky was also subtracted in this step.

---

[1] This problem was later reported in the September 2009 issue of the WFC3 Space Telescope Analysis Newsletter (STAN); see *http://www.stsci.edu/hst/wfc3/documents/newsletters/STAN_09_01_2009*. This problem was fixed in the latest CALWF3 (Version 1.7).

[2] We note that a multiplicative correction of this kind was not made in Bouwens et al. (2010), Oesch et al. (2010) or Bunker et al. (2009), and this may have contributed to the differences in photometry. McLure et al (2010) treated the four quadrants independently and thus avoided this problem (A. Koekemoer, priv. comm.).

3.2 Image Mosaicking

We used the MultiDrizzle software (Koekemoer et al. 2002), which was distributed in the STSDAS.DITHER package (Version 2.3; May 11, 2009), to correct for geometric distortion and to stack the individual images. MultiDrizzle is a Python wrapper that streamlines the processing of *HST* images using the Drizzle algorithm of Fruchter & Hook (1997, 2002) to optimally recover spatial resolution by subpixel resampling. While its implementation for handling the new WFC3 data is still understandably preliminary at this stage, it has served our main purpose well, although we had to make quite a number of manual adjustments.

A critical part of this step is to correct for geometric distortion, which affects essentially everything including cosmic-ray rejection, astrometric accuracy and photometry. We used the latest distortion parameter table (IDCTAB; made public on 2009 September 9) delivered by the WFC3 instrument team, which was derived based on the in-flight calibration observation on 2009 July 23. While this calibration was done only using H_{160}, the polynomial representations are the same for all bands and thus are taken as universally applicable in the IDCTAB. We note that McLure et al. (2010) used the same IDCTAB as we did, while Oesch et al. (2010), Bouwens et al. (2010) and Bunker et al. (2009) derived their own geometric distortion solution using the HUDF ACS data as the reference.

As usual, images obtained during different visits still have non-negligible offsets in their World Coordinate System (WCS) after correction for the geometric distortion. This is mainly caused by the intrinsic astrometric inaccuracies of the guide stars used in different visits. If this were not corrected, MultiDrizzle would not properly identify the cosmic-ray hits, or would incorrectly flag real objects as cosmic rays. More critically, the individual images would not be aligned and thus would not result in a useful stack. To solve this problem, we used the HUDF ACS images as the astrometric reference and calculated the transformation that should be applied to each *distortion-corrected* image. About 11–12 common objects were manually identified in each input image and the reference ACS z_{850} image, and we solved for X-Y shift, rotation, and plate scale. Here the ACS image was 3×3 rebinned, giving a spatial resolution of $0.09''$ pix^{-1}. This scale would be the plate scale of our final WFC3/IR stacks, and was chosen for a good reason. We would like to obtain a better spatial resolution offered by the subpixel-dithered observations, and at the same time we do not want to lose sensitivity to low surface brightness objects because of excessive subsampling. The chosen scale is a well matched compromise of all factors considered.

These transformations were then passed to MultiDrizzle, and the drizzling process was re-run to put each input image onto the pre-specified grid. We set the drizzling scale ("pixfrac") to 0.8. Cosmic-ray hits were identified and excluded from stacking. We inspected the few images that were affected by the image persistence, and verified that the affected pixels were flagged in the masks and did not enter the combining process. The end results were mosaics and associated weight images in three bands, all aligned with the 3×3 rebinned ACS images. By comparing the positions of point-like sources in the ACS images and in our mosaics, we conclude that the astrometry of the latter is good to ~ 0.5 pixel ($0.045''$) on average; we expect that this can be further improved after better geometric distortion coefficients are available. Figure 2 shows a color composite of the field, using the ACS B_{435} as blue, ACS i_{775} as green, and a weighted mean of all three WFC3/IR bands as red.

We note that McLure et al. (2010) also used the standard MultiDrizzle to generate mosaics, and they adopted a final scale of $0.03''$ pix^{-1}. Oesch et al. (2010) and Bouwens et al. (2010) used their own version of the modified MultiDrizzle, and adopted a final scale of $0.06''$ pix^{-1}. Bunker et al. (2009) did not use the drizzle algorithm but combined the individual images after using IRAF GEOMAP and GEOTRAN tasks to map them to the same astrometric grid of a $0.06''$ pix^{-1} scale.

4 CATALOG CONSTRUCTION

The selection of dropouts relies on comparing photometry of sources in successive passbands. Our photometry procedure, which is optimized for this purpose, is described below in detail.

4.1 Photometry

We carried out matched-aperture photometry by running the SExtractor program of Bertin & Arnouts (1996) in the dual-image mode. The three WFC3/IR mosaics were used in turn as the detection images to prepare catalogs for dropout selection at different redshifts. Hereafter, we will refer to these catalogs as the Y_{105}-based, J_{125}-based and H_{160}-based catalogs, respectively. Our photometric zeropoints were from the latest delivery of the WFC3 instrument team on 2009 September 9; in the AB system, these are 26.27, 26.25 and 25.96 mag in Y_{105}, J_{125} and H_{160}, respectively[3].

The drizzle-combined images have correlated pixel noise because of the subpixel sampling. This correlation should be taken into account when estimating photometric errors of measured sources. We followed the procedure utilized in the GOODS program (Dickinson et al. 2004) to calculate the correlation amplitudes in our mosaics, and then to derive the so-called "RMS maps" that describe the absolute root-mean-square noise of each pixel. We found that the actual noise would be underestimated in the WFC3 mosaics by a factor of 1.2–1.7 if the correlation were not properly taken into account. A similar procedure was applied to the rebinned ACS images as well, because the rebinning also changed the pixel noise properties. The resulting RMS maps were supplied to SExtractor to estimate background fluctuation at the source detection phase and to calculate photometric errors at the extraction phase. We have also estimated the depths of the WFC3/IR mosaics using these RMS maps. The 5-σ depths within a $0.2''$-radius aperture are 28.52, 28.85 and 28.94 mag in Y_{105}, J_{125} and H_{160}, respectively. We note that these values are generally consistent with the depths quoted in other works. However, they do not completely agree – our estimates tend to be slightly shallower. The differences could be due to two major reasons. One reason is the slight difference in zeropoints used, which we will discuss further in the next section. The other is the differences in the methods used to measure the correlated noise; underestimating the correlation noise would result in artificially deeper limits and artificially higher signal-to-noise ratios (S/N).

The SExtractor runs were set to output two different flavors of magnitudes, namely, MAG_AUTO and MAG_ISO. The default SExtractor parameter settings for MAG_AUTO use a Kron factor of 2.5 and a minimum radius of 3.0 pixels, and the resulting MAG_AUTO values are generally considered as total magnitudes. Since we are mostly interested in faint objects for this study, we set these parameters to (Kron factor, minimum radius)=(1.2, 2.0). This results in small apertures for the MAG_AUTO measurement, which, while losing a non-negligible amount of light for bright objects, is optimal for high S/N extraction of faint sources. With these settings, the MAG_AUTO magnitudes are quite similar to MAG_ISO, except that at the very faint levels the latter usually result in better S/N as their extraction apertures tend to be smaller. We compared the MAG_AUTO values with these two different settings for the sources that are brighter than 22.0 mag and found a systematic offset of 0.16 mag. We thus add -0.16 mag to correct the MAG_AUTO values obtained with small Kron parameters to total magnitudes.

A 2-pixel, 5×5 Gaussian filter was used in these SExtractor runs for source detection. The detection threshold was set to 0.8-σ above the filter-convolved image, and a minimum of two connected pixels above the threshold was required. For an extracted source to be included in the final catalog, it is required to have S/N≥ 3 in the detection band, calculated within either the MAG_AUTO aperture *or* the MAG_ISO aperture. Excluding the noisy field edges, our final Y_{105}-based, J_{125}-based and H_{160}-based catalogs include 2475, 2945 and 3156 sources, respectively. In contrast, Bunker et al. (2009) quoted much more conservative extraction criteria and yet reported ~ 4000 sources in their Y_{105}-based catalog.

Figure 3 presents the source surface densities in these three bands inferred from our catalogs. For comparison, the source surface density derived from the z_{850}-based catalog of YW04b is also shown. All these curves agree with each other very well up to AB=29.2 mag (indicated by the vertical dotted line). Beyond this point, the Y_{105} count drops slightly faster than the z_{850} count, while the J_{125} and

---

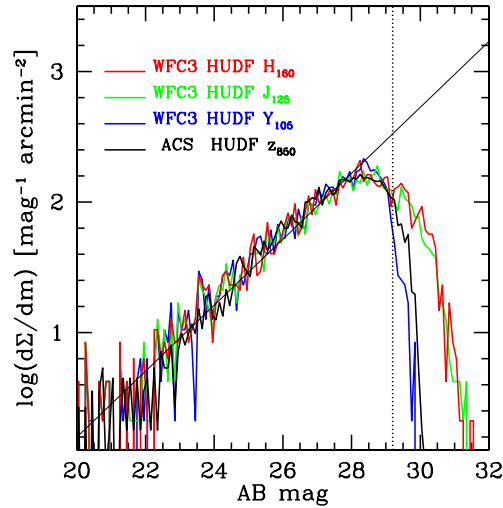[3] See *http://www.stsci.edu/hst/wfc3/phot_zp.lbn* and also the WFC3 STAN September 2009 issue.

Fig. 3 Source surface densities in the three WFC3 passbands, derived using the source counts from the Y_{105}-, J_{125}- and H_{160}-based catalogs, respectively. For comparison, the black curve shows the source surface density in the ACS z_{850}-band, derived using the HUDF z_{850}-based from YW04b. In all cases, only sources with S/N≥ 3 are used. The vertical dotted black line is at AB=29.2 mag, beyond which the J_{125}- and H_{160}-based catalogs seem to start to suffer from contamination. We limit our analysis to the regime brighter than this limit. For reference, the thin straight line indicates a power-law fit to the part where the counts are complete.

H_{160} counts appear to be much higher than the z_{850} count, which seems to suggest that source contamination becomes a problem. Therefore, we limit the candidate search to $AB \leq 29.2$ mag. When interpreting our results later in the paper, we further limit our discussion to $AB \leq 29.0$ mag (see Sect. 6).

4.2 Zeropoints

While Oesch et al. (2010) and Bouwens et al. (2010) have used the same WFC3 magnitude zeropoints as we did, Bunker et al. (2009) and McLure et al. (2010) have used different methods to derive their own zeropoints. These different approaches all involve using either the NIC3 or the VLT/ISAAC observations in this area. In this section, we examine to what extent these existing observations are consistent with the new WFC3 data in terms of zeropoints.

The ISAAC mosaics and their zeropoints used here are from the ESO GOODS/ISAAC final data release (Version 2.0) as of 2007 September 10 (Retzlaff et al. in prep.), which were based on the data obtained under Programs LP168.A-0485. We only compared to the ISAAC J-band, as this passband is close to the WFC F125W-band (see the bottom-left panel of Fig. 4). We used MAG_AUTO, and the photometry of the ISAAC image was done using (Kron factor, minimum radius)=(2.5, 1.2) and hence the obtained MAG_AUTO can be treated as total magnitudes. As mentioned earlier, we already added -0.16 mag to our WFC3 photometry to correct for total magnitudes. The comparison of WFC3(125W) vs. ISAAC(J) is shown in the top-left panel of Figure 4. The average offset is ~ 0.04 mag, suggesting that a proper zeropoint can be obtained in this band by using the ISAAC J-band as reference.
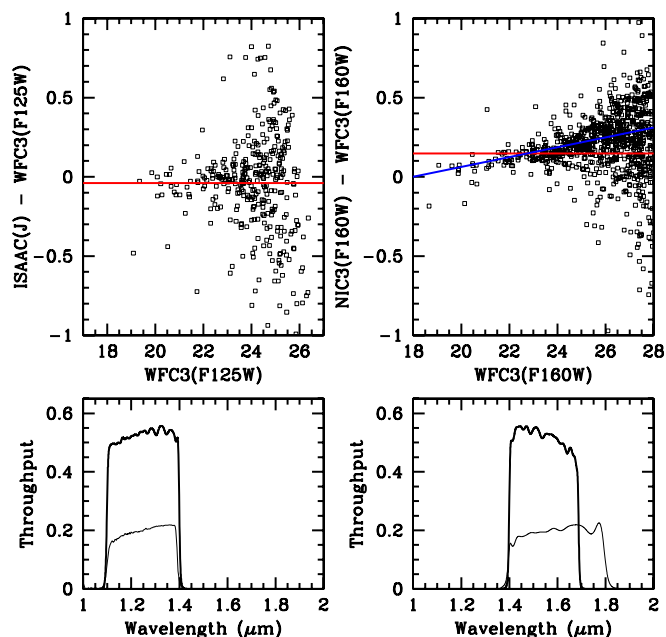
Fig. 4 Magnitude zeropoint comparisons to those using the VLT/ISAAC images (*left*) or the NIC3 images (*right*) as references. Only comparisons to the ISAAC J-band and the NIC3 F160W-band are made, since the shapes of these two passbands (*thin lines in the bottom panels*) are reasonably close to WFC3 F125W and F160W (*thick lines in the bottom panels*), respectively. While the ISAAC J-band magnitudes appear to be -0.04 mag too bright on average (*indicated by the horizontal line in the top left panel*), the NIC3 F160W-band magnitudes are $+0.15$ mag too faint (*indicated by the horizontal line in the top right panel*) if using the zeropoint of Thompson et al. (2005). In addition, the offset of the NIC3 F160W-band magnitudes shows a general trend with respect to source brightness (*as shown by the blue line*), indicative of a significant non-linearity in the NIC3 zeropoint calibration.

The NIC3 mosaics used here are the Version 2 products of Thompson et al. (2005), which are registered to exactly the same astrometric grid and have the same pixel scale as ours (i.e., using the 3×3 rebinned HUDF ACS images for reference). We only compared our F160W image to their F160W one, as the two passbands are reasonably close to each other. We did not compare to their F110W band, because the latter is much wider than either the WFC3 F105W or F125W and thus a straightforward comparison would be difficult. We ran SExtractor in the dual-image mode with the same parameter settings as described above, using their NIC3 mosaic as the detection image. The comparison between WFC3(F160W) and NIC3(F160W) is given in the right panel of Figure 4. The offset between the two sets amounts to ~ 0.15 mag (with NIC3 magnitudes being too faint). Similar results have been reported by Coe et al. (2006), who quote a zeropoint offset of 0.18 mag in NIC3(F160W). In addition, a significant trend of non-linearity in the NIC3 magnitudes can be clearly seen in Figure 4. This non-linearity was not determined until 2006 (see NICMOS ISR 2006-001 & 002), and therefore was not removed from the NIC3 HUDF data. Caution should be taken when using the NIC3 images for zeropoint determination.

4.3 Photometry of Other Groups

As different approaches to photometry can result in different catalogs and thus impact the candidate selection, for comparison purposes we summarize here the methods and some important settings that were used in the other four papers.

Bunker et al. used the thermal-test zeropoints of 26.16, 26.10, and 25.81 mag in these three bands, which are 0.11, 0.15 and 0.15 mag too bright, respectively. McLure et al. derived their own zeropoints using ground-based near-IR observations and also the NICMOS F160W-band image, and obtained zeropoints of 26.25, 26.25 and 26.10 mag in Y_{105}, J_{125} and H_{160}, respectively. These are very close to the in-flight zeropoints that we used; the offsets are -0.02, 0.00 and 0.04 mag in these three bands, respectively.

All groups except McLure et al. have used SExtractor in dual-image mode for both the rebinned ACS and the WFC3 IR images. Bouwens et al. used the χ^2-combined J_{125} and H_{160} image as the detection image. They used a small Kron factor of 1.2 as we did, but corrected these magnitudes to total magnitudes on a source-by-source basis. Finally, they added an overall correction of -0.1 mag to account for light on the wings of the PSF. Oesch et al. used the summed Y_{105} and J_{125} image as the detection image, and used a Kron factor of 2.5 to define the apertures. They also added a final correction of -0.1 mag. For comparison, we did not apply this -0.1 mag correction. Bunker et al. used their Y_{105}, J_{125} and H_{160} mosaics as the detection images for the z_{850}-, Y_{105}- and J_{125}- dropout selections, respectively, similar to what we did. They used a fixed aperture of $r = 0.3''$ for flux measurement. McLure et al. performed photometry on the three bands independently, and used a fixed aperture of $r = 0.3''$.

All these subtle differences, in addition to the differences in the data reduction, contribute to the differences in the photometric results of different groups, especially at very faint levels.

5 DROPOUT SELECTION AND SAMPLES

We have mainly used the Y_{105}-, J_{125}- and H_{160}-based catalogs to select z_{850}-, Y_{105}- and J_{125}- dropouts as candidate galaxies at $z \approx 7$, 8 and 10, respectively. We have used a "$J_{125}+H_{160}$" image to improve the completeness of the Y_{105}-dropouts. This section presents the details of the selection and the dropout samples. While our catalogs include both MAG_AUTO and MAG_ISO, the latter is only for the purpose of quality control; MAG_AUTO is used throughout the remainder of this paper.

5.1 Selection of z_{850}-dropouts

Our major color criterion for the z_{850}-dropout selection is $z_{850} - Y_{105} \geq 0.8$ mag, which selected candidates at $6.4 \leq z \leq 7.7$. We synthesized a large number of galaxy templates based on the model of Bruzual & Charlot (2003), and found that one should use the criterion of $z_{850} - Y_{105} \geq 1.0$ mag to select galaxies at $z \gtrsim 6.6$. Lowering this threshold to $z_{850} - Y_{105} \geq 0.8$ mag is appropriate for including galaxies at $z \approx 6.5$. Because the i_{775}-dropout selection for galaxies at $5.5 \lesssim z \lesssim 6.5$ loses its efficiency at $z \approx 6.5$ where the Lyman-break signature is starting to move out of the z_{850}-band, we decided to adopt $z_{850} - Y_{105} \geq 0.8$ mag in order to obtain a more complete census of high-redshift galaxies. In addition to the above criteria, we required that a candidate should be undetected (S/N< 2) in the other ACS bands (i_{775}, V_{606} and B_{435}). The color-color diagram shown in Figure 5 demonstrates our selection. We did not place a constraint on the $Y_{105} - J_{125}$ color, as it depends on the intrinsic properties of the galaxy that we do not know *a priori*. While this could potentially result in slightly more contamination from very cool Galactic brown dwarfs and some very red galaxies at lower redshifts, our procedure below largely eliminates this concern.

The WFC3 and ACS images of the candidates selected in the first step were all visually inspected to make sure that these are real objects and that their photometry is not corrupted for any complicated reasons that cannot be handled by SExtractor. During this step, any extremely compact sources
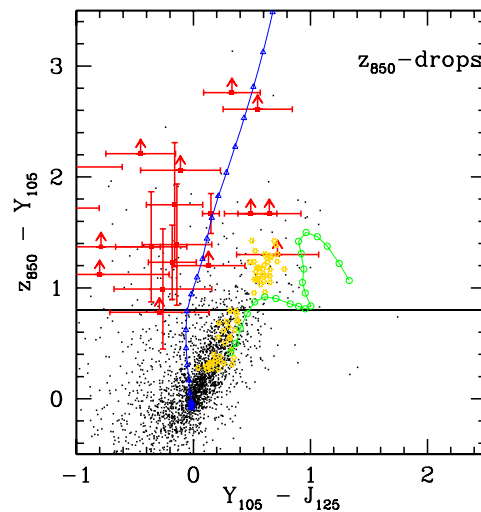
Fig. 5 Color-color diagram demonstrating the selection of z_{850}-dropouts. The black dots are field objects, and the horizontal line indicates the major color selection criterion of $z_{850}-Y_{105} \geq 0.8$ mag. The red data points with error bars are the selected candidates. The yellow symbols show the colors of M-, L- and T-dwarfs, which are calculated using the spectra from Leggett et al. (2000), while the green symbols show the colors of a typical red galaxy at $z \approx 1$–3 simulated using BC03 models. The blue symbols show the color track of a typical young galaxy at high redshift; at $z \gtrsim 6.5$ it passes above the selection threshold.

would be flagged as possible brown dwarfs; we found no such source in our case here. Following Yan et al. (2006), we also used the GOODS *Spitzer* IRAC images for further rejection of possible contaminators from the red galaxy populations at low redshifts ("IRAC-selected Extremely Red Objects;" Yan et al. 2004). For all the non-blended cases in the IRAC images where we would have no ambiguity in identifying counterparts, we found no such contaminators. A total of 21 candidates have survived after this culling process.

Figure 6 shows the image stamps of these z_{850}-dropouts, and Table 1 lists their positions and photometries. These sources have Y_{105} magnitudes ranging from 26.20 to 29.15 mag. All but one of them have $z_{850} - Y_{105} \geq 1.0$ mag, indicating that they are likely at $z \gtrsim 6.6$. We note that four objects in Table 1 have been previously selected as z_{850}-dropouts by various groups using the HUDF NIC3 data. ID zdrop-A032, the second brightest case in Table 1, is one of the few earliest z_{850}-dropouts reported, and was first published by YW04b (ID No. 3). We will discuss this source further together with some other objects in Table 1 later in Section 6.

Oesch et al. (2010) reported 17 z_{850}-dropouts using similar (but not the same) color criteria, 14 of which are also in our sample. These common objects are listed in the first part of Table 1. Three of their dropouts escape our selection for various reasons. One of these objects, their ID UDFz-38537519, is very faint in all our WFC3 images and falls below our S/N$\geq$ 3 threshold. One other object, their ID UDFz-36777536, has $z_{850} - Y_{105} = 0.73$ mag in our catalog and thus was not selected by our criteria. The last one, their ID UDFz-37807405, which is likely a genuine z_{850}-dropout, was "vetoed" by ACS photometry in our catalog. This source is very close to the brightest star in the HUDF, and SExtractor reports S/N$>$ 5 detections in the ACS V_{606} and i_{775} bands because the strong light gradient caused by this star badly skews the background estimate at the source location in the ACS images, resulting in an error in our ACS photometry for this source.

Table 1 Properties of Galaxy Candidates at $z \approx 7$[a]

ID zdrop-	RA	Dec(J2000)	z_{850}	Y_{105}	J_{125}	H_{160}	$z-Y$	$Y-J$	$J-H$	Cross.Ref. & ID[b]
A032[c]	3:32:42.560	−27:46:56.593	27.94±0.17	26.27±0.06	26.12±0.04	26.14±0.04	1.67	0.15	−0.02	1(42566566); 3(zD1); 4(688)
A025[d]	3:32:38.798	−27:47:07.120	>29.95	27.19±0.21	26.86±0.12	26.74±0.10	>2.76	0.33	0.12	1(38807073); 3(zD2); 4(835)
A008[d,e]	3:32:42.563	−27:47:31.578	>29.93	27.32±0.27	26.77±0.12	26.84±0.12	>2.61	0.55	−0.07	1(42577314); 3(zD3); 4(1144)
A060	3:32:43.147	−27:46:28.474	>29.80	27.59±0.20	28.04±0.22	27.69±0.15	>2.21	−0.45	0.35	1(43146285); 3(zD5); 4(1678)
A017	3:32:41.044	−27:47:15.529	>29.96	27.90±0.26	28.01±0.22	28.20±0.24	>2.06	−0.11	−0.19	1(41057156); 4(2066)
A016	3:32:36.380	−27:47:16.199	29.41±0.45	28.04±0.21	28.40±0.22	28.37±0.20	1.37	−0.36	0.03	1(36387163); 3(zD6); 4(1958)
A033	3:32:39.577	−27:46:56.449	29.95±0.53	28.20±0.18	28.36±0.16	29.10±0.28	1.75	−0.16	−0.74	1(39586565); 4(1915)
A014[d]	3:32:39.556	−27:47:17.534	>29.87	28.20±0.20	27.71±0.10	27.70±0.09	>1.67	0.49	0.01	1(39557176); 3(zD4); 4(1092)
A040	3:32:37.442	−27:46:51.226	29.44±0.30	28.21±0.15	28.39±0.14	28.57±0.15	1.23	−0.18	−0.18	1(37446513); 4(1880)
A044[f]	3:32:44.703	−27:46:44.245	>29.88	28.21±0.25	27.56±0.10	27.59±0.10	>1.67	0.65	−0.03	1(44716442); 3(zD7); 4(1107)
A003	3:32:37.209	−27:48:06.106	>29.91	28.61±0.33	27.89±0.12	28.21±0.16	>1.30	0.72	−0.32	1(37228061); 3(zD9); 4(1574)
A047	3:32:40.563	−27:46:43.590	30.15±0.50	28.76±0.22	28.90±0.20	29.33±0.27	1.39	−0.14	−0.43	1(40566437); 3(zD8); 4(2206)
A057[g]	3:32:39.730	−27:46:21.295	>29.93	29.15±0.30	29.44±0.30	29.50±0.30	>0.78	−0.29	−0.06	1(39736214); 3(zD10); 4(2502)
A046[f]	3:32:44.739	−27:46:44.879	>29.87	27.78±0.26	29.05±0.61	28.39±0.30	>2.09	−1.27	0.66	4(2888)
A053	3:32:38.360	−27:46:11.849	>29.93	28.73±0.26	28.60±0.17	28.74±0.18	>1.20	0.13	−0.14	3(zD11)
A056	3:32:38.650	−27:46:16.381	>29.93	28.21±0.25	29.90±0.85	29.23±0.42	>1.72	−1.69	0.67	
A052	3:32:41.824	−27:46:11.204	>29.90	28.53±0.27	29.32±0.43	29.23±0.36	>1.37	−0.79	0.09	
A055	3:32:42.656	−27:46:22.616	>29.90	28.62±0.29	—	29.20±0.33	>1.28	—	—	
A062	3:32:37.345	−27:46:28.510	>29.92	28.80±0.32	29.60±0.50	29.70±0.50	>1.12	−0.80	−0.10	
A065	3:32:36.519	−27:46:41.995	29.98±0.45	28.99±0.30	29.25±0.29	29.73±0.41	0.99	−0.26	−0.48	4(2940)
A007[h]	3:32:34.530	−27:47:35.938	>29.93	26.20±0.03	26.05±0.02	25.88±0.02	>3.73	0.15	0.17	1(34537360); 3(zD0)

[a.] All magnitude limits are 2-σ limits measured within an $r = 0.2''$ aperture. [b.] Cross References: 1 – Oesch et al. (2010); 3 – Bunker et al. (2009); 4 – McLure et al. (2009); numbers in parentheses are their corresponding IDs. [c.] Detected in the NIC3 HUDF data; first reported in YW04. [d.] Detected in the NIC3 HUDF data; first reported in Bouwens et al. (2004). [e.] This object happens to be very close to a Y_{105}-dropout (see Table 2, ID z8-B041); Oesch et al. (2010) seem to treat them as one object. [f.] These two objects are separated by $0.79''$; using their z_{ph} of ~ 7.0 (see Table 5), this separation corresponds to a proper length of ~ 4.2 kpc. [g.] This source is at the border line of selection. See text for discussion. [h.] This bright object is likely a variable source. See Fig. 7 for its light curve.
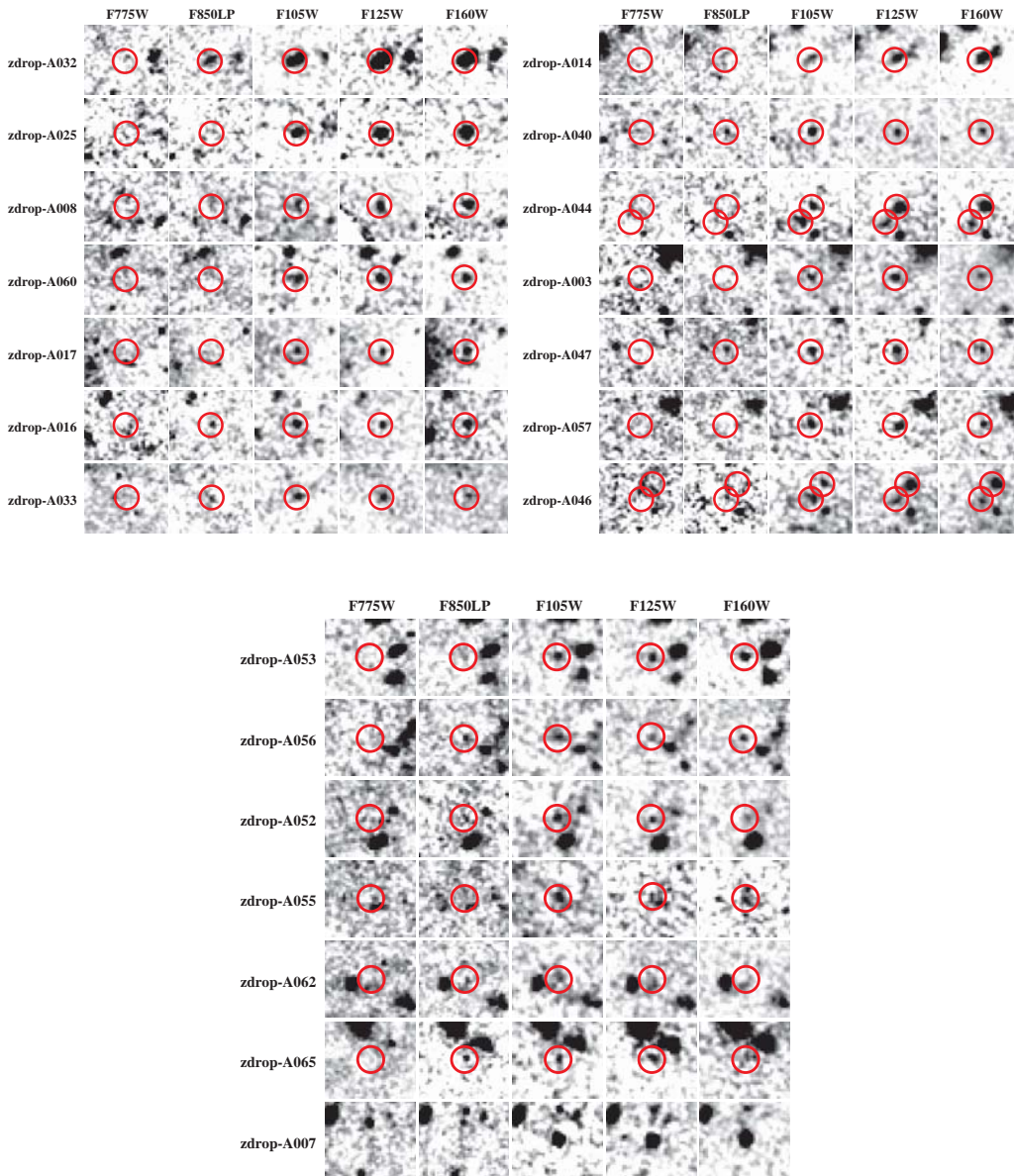
Fig. 6 ACS and WFC3/IR image stamps of $z \approx 7$ galaxy candidates in the HUDF, centered on the source locations. These objects are selected as z_{850}-band dropouts. Images are $2.7'' \times 2.7''$ in size; north is up and east is left. The red circles are $0.5''$ in radius. Object A032 shows clear double-nucleus morphology, which is indicative of a merging event. Note that ID A044 and 046 are close neighbors, which might be physically associated. ID zdrop-A007 is probably a transient object rather than a genuine $z \approx 7$ galaxy; it is shown here for completeness.
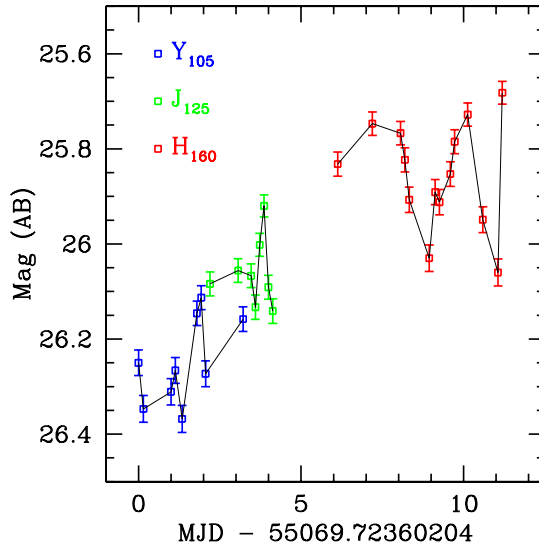
Fig. 7 Light curves of the possible transient object zdrop-A007. The blue, green and red data points are its magnitudes in Y_{105}, J_{125} and H_{160}, respectively. These magnitudes were measured on the drizzle-combined mosaics made from the images of individual visits (consisting of two orbits for each exposure). This object is excluded from further analysis.

Seven of our dropouts are not included in Oesch et al. (2010), all of which have $Y_{105} < 29.0$ mag in our catalog. One of them, zdrop-A053, is included in the sample of Bunker et al. (2009; their ID zD11). Two other objects, our zdrop-A046 and A065, are included in the sample of McLure et al. (2010; their IDs 2888 and 2940, respectively). The remaining four, zdrop-A056, A052, A062, and A055, are not reported elsewhere. These seven sources are 3.4–4.3 σ detections in our Y_{105} mosaic, although most of them only have S/N< 3 in the current J_{125} and H_{160} data (except zdrop-A065 which is detected at S/N= 3.7 in J_{125}). We expect that these dropouts will be detected at high significance once the remaining 68% of the allocated orbits for program GO-11563 are taken in 2010.

McLure et al. (2010) have reported six additional candidates at $6.6 \leq z \leq 7.8$ that are neither in our z_{850}-dropout sample nor in that of Oesch et al. (2010). One of them is actually in our J_{125}-dropout list, which we will discuss later. Their object ID 2794 is not likely a valid candidate, as it is clearly seen in our 3×3-rebinned ACS B_{435} image. Two of their sources, IDs 2826 and 2487, did not enter our catalog because their locations are at the noisy field edges that were excluded from our photometry. Their ID 2395 was not selected by us because it has $z_{850} - Y_{105} = 0.792$ mag in our catalog. Lastly, their ID 1064, which is likely a valid candidate, escaped our selection because its ACS photometry in our catalog was contaminated by a close neighbor that is not seen in the WFC3 IR image.

Finally, we comment on the source zdrop-A007, which is the brightest one in Table 1. As also noted by others, this source is not present in the HUDF NIC3 images, although its present brightness (~ 26 mag) is well above the detection limits of those images. Therefore, it must be a highly variable object. To further explore this possibility, we drizzle-combined the images from each visit separately, and examined this source in each visit. It is consistent with being a point-source throughout. We measured its magnitudes in all three passbands as a function of time, using a circular aperture of
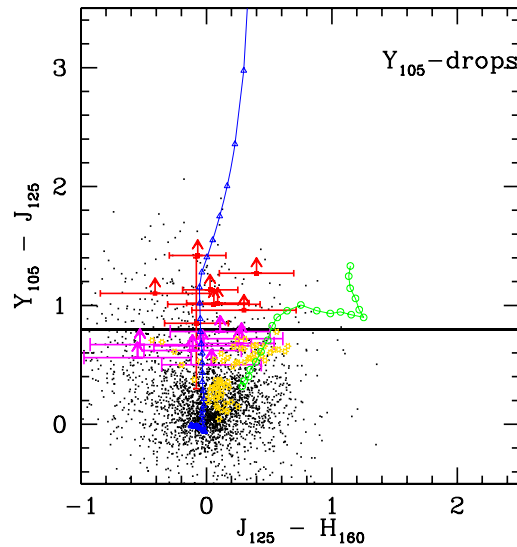
Fig. 8 Color-color diagram for the Y_{105}-dropout selection, similar to Fig. 5. The magenta symbols are the candidates that do not satisfy $Y_{105} - J_{125} \geq 0.8$ mag when using the $1\,\sigma$ upper limits in Y_{105} for the non-detections in this band.

5-pixels in radius. The results are given in Figure 7, which clearly show that its brightness indeed was varying in all three passbands over the period of these observations. However, the amplitude of variation is ~ 0.5 mag at most, which still makes it difficult to explain its absence from the NIC3 images, unless it is a transient object. As currently we have no constraint on its redshift, we exclude this object from further discussion in this paper.

5.2 Selection of Y_{105}-dropouts

We first selected Y_{105}-dropouts using the J_{125}-based catalog. The main color criterion is $Y_{105} - H_{160} \geq 0.8$ mag, which is appropriate for identifying the Lyman-break signature at $7.7 \leq z \leq 9.4$. Valid candidates should not be present in any ACS passbands at S/N> 2. No constraint was put on their $J_{125} - H_{160}$ colors. Objects that meet these criteria were visually inspected on all the ACS, WFC3 and *Spitzer* IRAC images to exclude contamination from spurious detections and interlopers at low redshifts. In total, 10 Y_{105}-dropouts were selected to $J_{125} \leq 29.0$ mag. All the five Y_{105}-dropouts reported in Bouwens et al. (2010) have been recovered, and we have found another five more from this analysis.

Because only $\sim 44\%$ of the J_{125}-band observations have been finished in the first epoch, one wonders what deeper observations could be added to the result. Therefore, we also made a composite "JH" image by weight-combining the J_{125} and H_{160} mosaics, and used this new "JH" image as the detection image to generate a "JH"-based catalog for Y_{105}-dropout selection. For an object to be included in this catalog, it was required to have final extracted S/N≥ 3 in either J_{125}-band or in H_{160}-band. As it turns out, this JH-based catalog includes about 9% more sources as compared to the J_{125}-based catalog.

We used this JH-based catalog to search for Y_{105}-dropouts in a similar way. Somewhat surprisingly, this process resulted in five new candidates. Close examination shows that they were all in the raw J_{125}-based catalog. Two of them were discarded because they do not have S/N≥ 3 as reported in
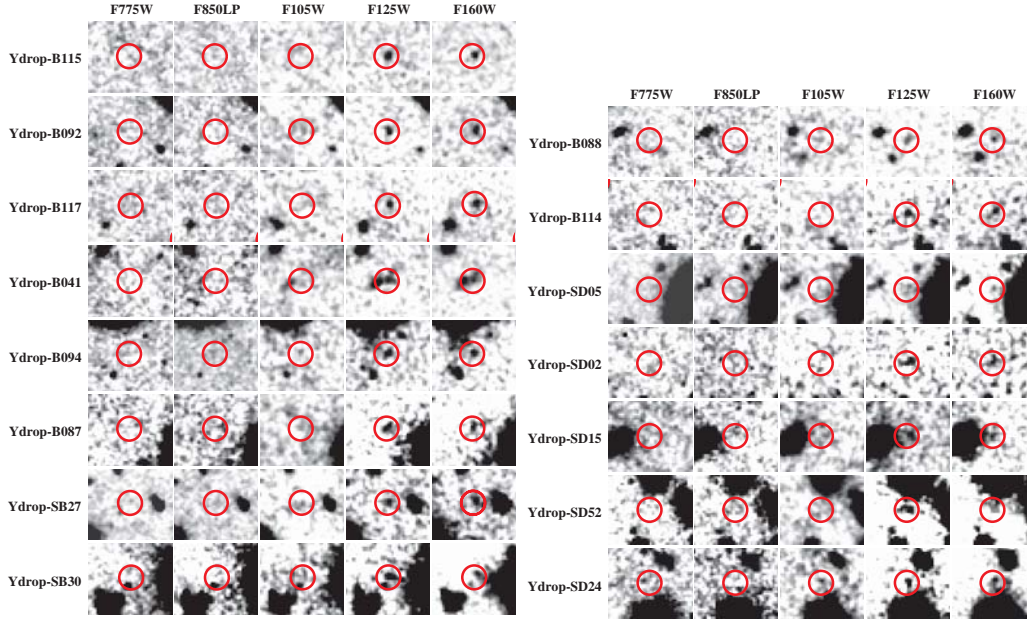
Fig. 9 Similar to Fig. 6, but for the selection $z \approx 8$ galaxy candidates.

the J_{125}-based catalog. The other three have S/N> 3 in the J_{125}-based catalog, but their extraction apertures were so defined (in the J_{125}-band mosaic) that their matched-aperture ACS photometry were contaminated by unrelated objects nearby and hence caused erroneously significant detections to be reported in the ACS bands. As a result, these three were not selected in the J_{125}-based search when applying our color criteria. On the deeper JH image, however, the extraction apertures for all these five objects were better defined, resulting in an improvement in their photometry that is significant enough to have them be selected as candidates.

Therefore, the total number of Y_{105}-dropouts now in our sample is 15. We point out that, while no constraint on the $J_{125} - H_{160}$ color was applied during selection, all the resulting candidates have $J_{125} - H_{160} \lesssim 0.4$ mag. Their locations in the color space are shown in Figure 8. We show their image stamps in Figure 9, and list their positions and photometric properties in Table 2. We also note that the formal $Y_{105} - J_{125}$ color limits of seven sources (the second part of Table 2, separated by the horizontal line), calculated using the formal 2-σ Y_{105}-band flux upper limits within an $r = 0.2''$ aperture, do not strictly meet the $Y_{105} - J_{125} \geq 0.8$ mag threshold. These include two sources in Bouwens et al., and one different source in Bunker et al. All the five additional JH-based candidates from our selection fall in this category. However, they only fall slightly short of the requirement; if we were instead to use a 1-σ limit as Bouwens et al. adopted, these sources would certainly go over the threshold. In addition, their $J_{110} - H_{160}$ colors agree with blue SEDs that are characteristic of star-forming galaxies. Therefore, we keep them in our sample, but will treat them differently when interpreting.

One of these sources, Ydrop-B041, is very close to a z_{850}-dropout, zdrop-A014. Oesch et al. (2010) identify both objects as one single z_{850}-dropout, their UDFz-39557176. Given its color lower limit of $Y_{105} - J_{125} > 1.4$ mag, we keep it in the Y_{105}-dropout sample. McLure et al. (2010) have included this object (their ID 1422) in their sample as well, and also separate it from B041 (their ID 1144) as we do. The other seven objects are not reported elsewhere.

Table 2 Properties of Galaxy Candidates at $z \approx 8$[a]

ID Ydrop-	RA	Dec (J2000)	z_{850}	Y_{105}	J_{125}	H_{160}	$z-Y$	$Y-J$	$z-J$	$J-H$	Cross.Ref. & ID[b]
B115	3:32:38.137	–27:45:54.018	> 29.92	> 29.52	28.39±0.17	28.36±0.14	—	> 1.13	> 1.53	0.03	2(38135539); 3(YD3); 4(1721)
B092	3:32:42.876	–27:46:34.525	> 29.79	29.30±0.52	28.45±0.18	28.53±0.18	> 0.49	0.85	> 1.34	–0.08	2(42886345); 3(YD1); 4(1765)
B117	3:32:37.800	–27:46:00.149	> 29.92	> 29.51	28.49±0.19	28.40±0.16	—	> 1.02	> 1.43	0.09	2(37796000); 3(YD2); 4(1939)
B041[c]	3:32:39.514	–27:47:17.387	> 29.84	> 29.50	28.08±0.16	28.15±0.16	—	> 1.42	> 1.76	–0.07	
B094	3:32:43.407	–27:46:36.077	> 29.95	> 29.49	28.22±0.25	27.82±0.16	—	> 1.27	> 1.73	0.40	
B087	3:32:42.416	–27:46:24.301	> 29.93	> 29.51	28.41±0.26	28.82±0.35	—	> 1.10	> 1.52	–0.41	
SB27	3:32:35.172	–27:47:16.966	> 29.82	> 29.55	28.54±0.28	28.48±0.24	—	> 1.01	> 1.28	0.06	
SB30	3:32:34.307	–27:47:11.476	> 29.85	> 29.51	28.55±0.34	28.25±0.24	—	> 0.96	> 1.30	0.30	
B088	3:32:43.081	–27:46:27.714	> 29.88	> 29.53	28.86±0.22	29.39±0.33	—	> 0.67	> 1.02	–0.53	2(43086276); 4(2841)
B114	3:32:37.635	–27:46:01.571	> 29.93	> 29.50	28.94±0.23	29.49±0.36	—	> 0.56	> 0.99	–0.55	2(37636015); 3(YD7); 4(2079)
SD05	3:32:36.532	–27:47:50.258	> 29.82	> 29.52	28.74±0.31	28.63±0.25	—	> 0.78	> 1.08	0.11	
SD02	3:32:37.583	–27:48:00.245	> 29.95	> 29.48	28.80±0.23	28.54±0.16	—	> 0.68	> 1.15	0.26	
SD15	3:32:38.409	–27:47:25.098	> 29.95	> 29.56	28.84±0.27	28.56±0.19	—	> 0.72	> 1.11	0.28	3(YD5)
SD52	3:32:38.809	–27:47:16.188	> 29.90	> 29.52	28.90±0.28	29.01±0.27	—	> 0.62	> 1.00	–0.11	
SD24	3:32:35.845	–27:47:17.156	> 29.95	> 29.54	29.04±0.30	29.00±0.26	—	> 0.50	> 0.91	0.04	

a. All magnitude limits are 2-σ limits measured within an $r = 0.2''$ aperture.
b. Cross References: 2 – Bouwens et al. (2010); 3 – Bunker et al. (2009); 4 – McLure et al. (2010); numbers in parentheses are their corresponding IDs.
c. This object consists of two components. It is very close to our ID z7-A008 and Oesch et al. (2010) take them as one object (their ID 39557176).

Two out of the seven Y_{105}-dropouts in Bunker et al. (2009) are neither in the sample of Bouwens et al. (2010) nor in ours. One object, their YD04, is too close to the noisy field edge and did not enter our catalog. Their YD06 did not match any object in our catalog within a $0.18''$-radius (or 2 pixels in our image). The closest object in our catalog lies $0.21''$ away; this object has a weak detection in the rebinned ACS B_{435} and V_{660} images and thus did not enter our sample. McLure et al. (2010) also report an additional source (their ID 2487) at $z \approx 7.8$; however this source is too close to the noisy field edge that is not considered in our photometry.

5.3 Selection of J_{125}-dropouts

As Figure 1 illustrates, galaxies at $z \approx 10$ can, in principle, be selected as J_{125}-dropouts. We carried out such a selection using the H_{160}-based catalog. The main criteria applied are $J_{125} - H_{160} > 0.8$ mag (Fig. 10), and S/N< 2 in the Y_{105}-band and in all the four ACS bands. This process selects candidates in $9.4 \lesssim z \lesssim 11.8$. As before, we visually inspected the candidates on all the ACS, WFC3, and IRAC images. In total, our selection has resulted in 20 J_{125}-dropouts for the $H_{160} = 29.0$ mag; all have S/N= 3.0–4.9 in the H_{160}-band. We list their locations and photometry in Table 3, and show their image stamps in Figure 11.

Table 3 Properties of Galaxy Candidates at $z \approx 10^{a}$

ID	RA	Dec (J2000)	z_{850}	Y_{105}	J_{125}	H_{160}	$J-H$
Jdrop-C067	3:32:43.291	–27:46:48.022	> 29.90	> 29.52	> 29.83	28.20 ± 0.25	> 1.62
Jdrop-C008	3:32:39.252	–27:48:02.603	> 29.95	> 29.54	> 29.81	28.28 ± 0.26	> 1.53
Jdrop-C027	3:32:35.073	–27:47:40.690	> 29.94	> 29.57	> 29.84	28.42 ± 0.22	> 1.42
Jdrop-C108	3:32:38.870	–27:45:38.632	> 29.92	> 29.27	> 29.64	28.52 ± 0.24	> 1.12
Jdrop-SC40	3:32:37.450	–27:46:14.250	> 29.91	> 29.49	> 29.85	28.54 ± 0.33	> 1.31
Jdrop-C071	3:32:39.588	–27:46:09.124	> 29.89	> 29.54	> 29.82	28.54 ± 0.28	> 1.28
Jdrop-C126	3:32:38.277	–27:46:05.315	> 29.93	> 29.53	> 29.82	28.55 ± 0.29	> 1.27
Jdrop-C020	3:32:38.127	–27:47:44.819	> 29.93	> 29.45	> 29.83	28.59 ± 0.29	> 1.23
Jdrop-C051	3:32:37.738	–27:47:04.888	> 29.88	> 29.51	> 29.83	28.60 ± 0.28	> 1.23
Jdrop-C114	3:32:35.168	–27:46:47.982	> 29.93	> 29.49	> 29.84	28.82 ± 0.24	> 1.02
Jdrop-C099	3:32:43.614	–27:46:35.162	> 29.85	> 29.52	> 29.83	28.83 ± 0.24	> 1.00
Jdrop-C047	3:32:41.754	–27:47:12.484	> 29.93	> 29.47	> 29.83	28.88 ± 0.26	> 0.95
Jdrop-C103	3:32:35.017	–27:46:40.073	> 29.88	> 29.54	> 29.83	28.89 ± 0.34	> 0.94
Jdrop-C030	3:32:36.648	–27:47:36.758	> 29.93	> 29.50	> 29.78	28.91 ± 0.31	> 0.87
Jdrop-C065	3:32:42.841	–27:46:48.954	> 29.90	> 29.49	> 29.82	28.92 ± 0.36	> 0.90
Jdrop-C061	3:32:43.007	–27:46:53.263	> 29.92	> 29.51	> 29.85	28.96 ± 0.30	> 0.89
Jdrop-C066	3:32:38.493	–27:46:48.608	> 29.94	> 29.47	> 29.78	28.97 ± 0.32	> 0.81
Jdrop-C106	3:32:36.582	–27:46:41.365	> 29.95	> 29.56	> 29.84	28.98 ± 0.30	> 0.86
Jdrop-C056	3:32:37.588	–27:46:58.451	> 29.94	> 29.51	> 29.82	29.01 ± 0.29	> 0.81
Jdrop-C034	3:32:39.255	–27:47:35.758	> 29.84	> 29.47	> 29.82	29.02 ± 0.25	> 0.80

[a.] All magnitude limits are 2-σ limits measured within an $r = 0.2''$ aperture.
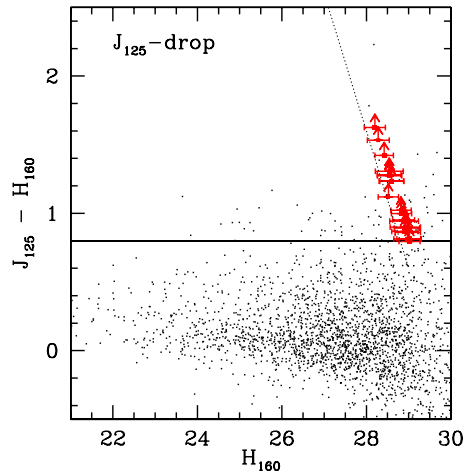

Fig. 10 Color-magnitude diagram for the J_{125}-dropout selection. The black dots are field objects, and the horizontal line indicates the major color criteria of $J_{125} - H_{160} \geq 0.8$ mag. The red data points are the selected candidates. Their positions are tilted (as indicated by the thin dashed line) because their 2-σ limits in J_{125} is ~ 29.8 mag.

While we only required that $J_{125} - H_{160} > 0.8$ mag, all these objects are undetected in the current J_{125} mosaic, making them single-band detections. One major concern about any single-band detections at or approaching the detection limit is whether they are real objects at all. In order to address this question, we performed two tests. We first visually examined every individual, distortion-
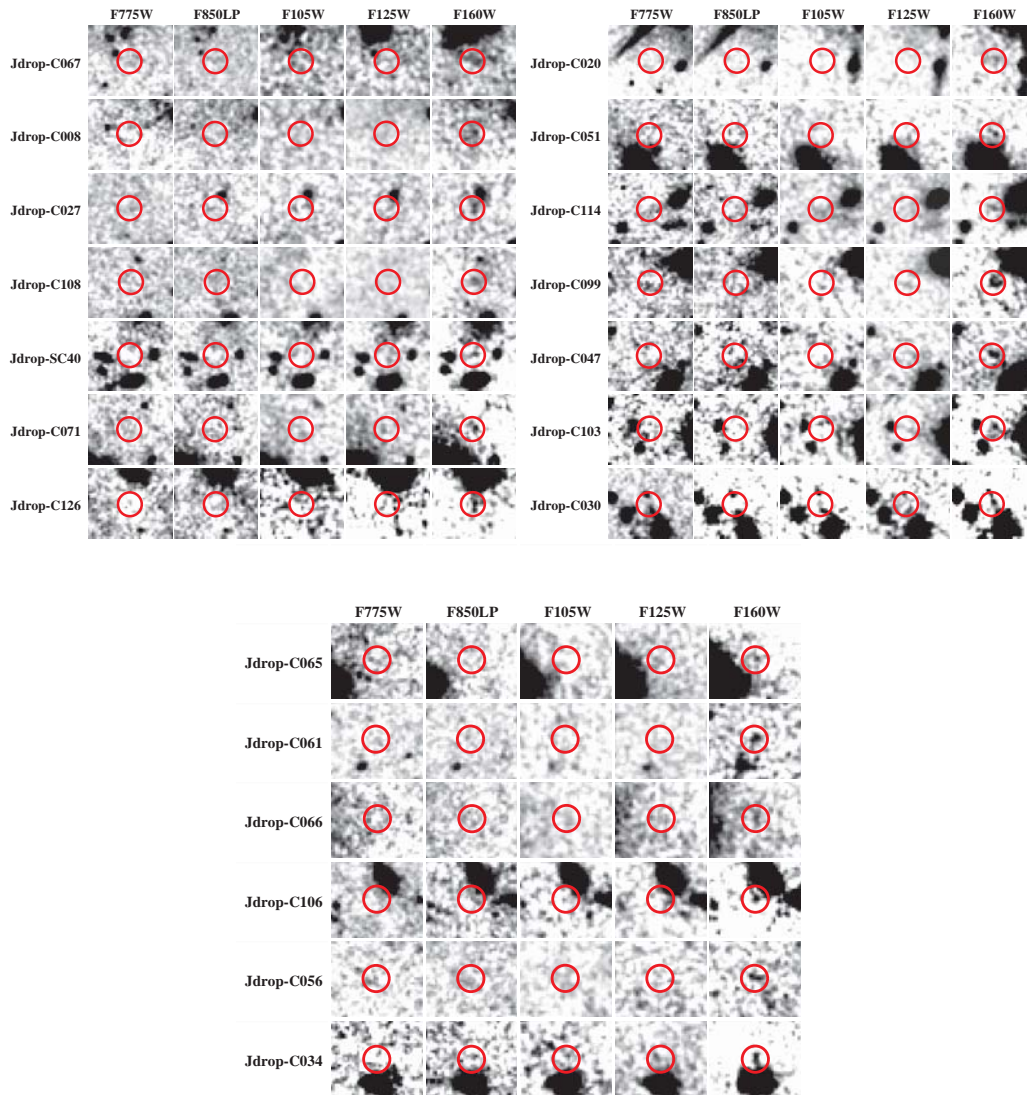
Fig. 11 Similar to Figs. 6 and 9 but for $z \approx 10$ galaxy candidates. Objects are selected as J_{125}-dropouts.

corrected H_{160}-band image and its associated pixel mask at the location of each candidate to see whether any of these objects could originate from residual cosmic-ray hits, other image defects, or any transients (such as asteroids). We did not find any evidence that this could be the case. We then broke the image set into two groups, each consisting of 28 images, and ran MultiDrizzle on these two subsets separately. This was done twice, first splitting the images by visits (i.e., the first group was made of the images from the first seven visits and the second group was made of the images from the later seven visits) and then splitting them by taking out half of the images from each visit. We then inspected the locations of our candidates, and found that they could still be seen in these mosaics that contain only half of the available data, albeit being weaker.
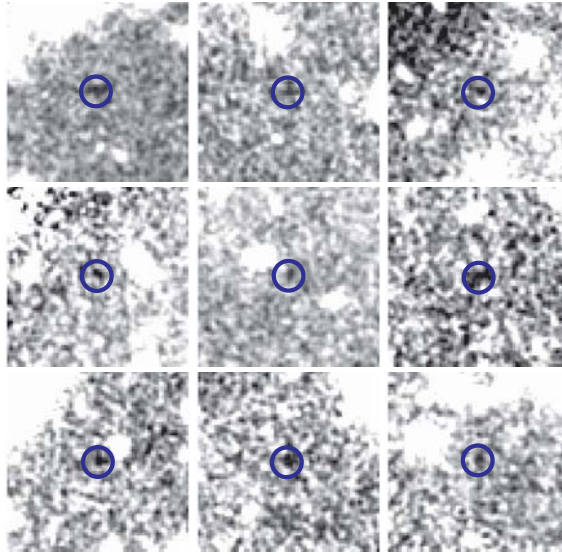
Fig. 12 Negative H_{160}-band image cutouts of the nine "negative candidates" that pass our J_{125}-dropout selection criterion in the "negative image" test. The cutouts are $6'' \times 6''$ in size. The blue circles are $0.5''$ in radius. The test suggests that our J_{125}-dropout sample could be contaminated at the level of 33%–47% due to noise fluctuation.

These tests strongly suggest that the H_{160}-band detections of our J_{125}-dropouts are the cumulative results of the weak but positive counts in the individual H_{160}-band images, which is characteristic of real objects. Strictly speaking, however, these tests still do not answer whether such a detection could be the cumulative result of the noise fluctuations in individual images that happen to be mostly positive in a few connected pixels. To address this issue, we carried out the so-called "negative image" test (e.g., Dickinson et al. 2004). The H_{160}-band mosaic, which has the mean background of zero by the way it was produced (see Sect 3.1), was multiplied by -1 to make any positive pixels become negative and vise versa. We then extracted "sources" in this negative image by running SExtractor in the same way as we did with the real H_{160} mosaic, including using the same RMS map. Because the noise fluctuation has the same probability of scattering a pixel to a negative value below the mean or to a positive value above the mean, the occurence of the "sources" in the negative image would represent spurious detections due to the noise fluctuation in the original image. The detected negative "sources" were further examined as if they were real candidate dropouts, and we found that nine of them would meet our selection criteria. The image cutouts of these nine "negative candidates" are shown in Figure 12. One of them would have $28.0 < H_{160} \leq 28.5$ mag, while the rest would have $28.5 < H_{160} \leq 29.0$ mag. Since our J_{125}-dropout sample has three objects in the former magnitude bin and 17 in the latter (see Table 3), these negative "dropouts" imply contamination rates of 33.3% and 47.1% in our sample in these two bins, respectively. We note that these are significantly lower than what Bouwens et al. (2009) estimated using a similar set of extraction parameters in their mosaics.

5.4 Compare to the Recent Result of Bouwens et al.

Recently, Bouwens et al. (2009) reported the result of their search for J_{125}-dropouts in this field. They have found a total of three J_{125}-dropouts, none of which are in our sample. They also claimed
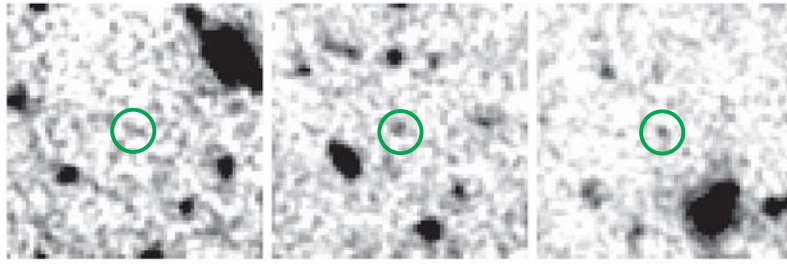
Fig. 13 Three J_{125}-dropouts of Bouwens et al. (2009) as seen in our H_{160}-band image. From left to right, these are their UDFj-43696407, UDFj-35427336 and UDFj-38116243. The cutouts are $6'' \times 6''$ in size; north is up and east is left. The green circles are $0.5''$ in radius. The first object is a non-detection in our image, and the other two have magnitudes fainter than our selection criteria. See text for details.

that the majority of our J_{125}-dropouts are implausibly too close to "bright, foreground galaxies," and hence questioned any of our J_{125}-dropouts being real.

We checked their three J_{125}-dropouts in our data. Figure 13 shows the cutout images at these locations in our H_{160}-band mosaic. Their UDFj-43696407, for which they reported $H_{160} = 28.9 \pm 0.2$ mag, turns out to be a formal non-detection in our image, and has a 2-σ upper limit within a $0.2''$-radius aperture of 29.91 mag. The other two objects, UDFj-35427336 and UDFj-38116243, are detected in our image, but have $H_{160} = 29.64\pm0.31$ and 29.70 ± 0.28 mag, respectively. As these are fainter than our adopted J_{125}-dropout selection threshold of $H_{160} \leq 29.2$ mag (see Section 4.1), they would not be included in our sample. We note that Bouwens et al. reported $H_{160} = 29.1 \pm 0.2$ and 28.9 ± 0.2 mag for these two objects, respectively.

We believe that such discrepancies could be partly explained by the differences in data reduction, which we already emphasized in Section 3. The two groups used different softwares and have adopted different approaches to process the data (e.g., reference files, registration, background subtraction, etc.), and it is very likely that there are also differences in the adopted parameters that could affect the results (e.g., drizzle scale, pixel scale, cosmic-ray rejection, weighting, etc.). It is not inconceivable that some differences in the mosaics would exist at the faintest level. For this reason, while the non-detection of one of their candidates is still puzzling, we do not exclude the possibility that the other two could be J_{125}-dropouts. The exclusion of these two objects from our sample, however, is demanded by our data and photometry. Even if future data show that their brightness agrees better with the photometry of Bouwens et al. than ours, their exclusion from our current sample still does not affect our major conclusion in Section 6. We know that the current data are significantly incomplete at $H_{160} \approx 29$ mag (see Fig. 3), and we expect our sample to be incomplete at this level. And this is precisely the reason that we have applied the incompleteness correction, as detailed in Section 6.3.

Bouwens et al.'s criticism that our candidates are spurious, however, is flawed. Their figure 7, based on which they claimed that our candidates are predominantly close to bright foreground sources, is not justified. It is not clear to us how they define "bright foreground sources," "blank sky" or "distance." While their "relative likelihood" is also not clearly defined, we believe that it is similar to a histogram normalized by total counts (but not entirely the same, since their "relative likelihood" does not add up to unity). Regardless of these ambiguities, their figure 7 concludes that the majority of our J_{125}-dropouts lie within $0.5''$ from "bright, foreground galaxies." We disagree with their assessment. In the image montages of the candidates shown in our current paper, including Figure 11 for the J_{125}-dropouts, the red circles used to indicate the source locations are always
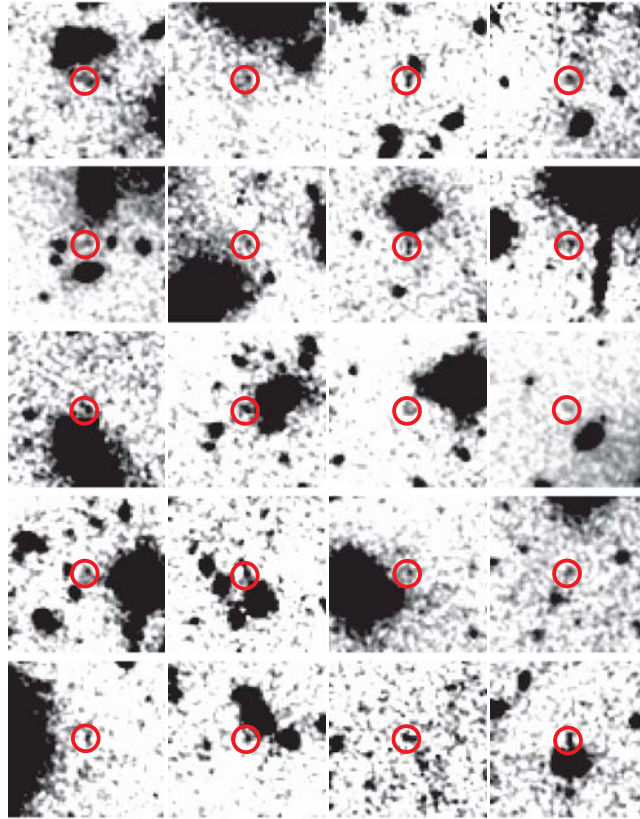
Fig. 14 H_{160}-band cutouts of all the 20 J_{125}-dropouts in our sample. From left to right and then from top to bottom, these objects are presented in the same order as shown in Table 3 and Fig. 11. The cutouts are $6'' \times 6''$ in size; north is up and east is left. The red circles are $0.5''$ in radius, which clearly show that most of these objects are $0.5''$ away from their bright neighbors, and thus fig. 7 of Bouwens et al. (2009) is misleading and incorrect.

$0.5''$ in radius, and one can see that the majority of our candidates do not have their red circles overlapped with any neighbor. To show this more clearly, Figure 14 displays the H_{160} image cutouts of all the 20 J_{125}-dropouts, in the order of their appearance in Table 3 (i.e., in decreasing H_{160}-band brightness). The cutouts are $6'' \times 6''$ in size, which is large enough to see the neighbors. We count six objects (30%) that have their red circles making contact with a bright neighbor (C106, C034, C030, SC40, C114, and C126), while Bouwens et al.'s figure 7 indicates that $\sim 90\%$ of our objects are within $0.5''$ from a bright neighbor, which is misleading. Similarly, their same criticism of our Y_{105}-dropouts which are not in common with theirs is also flawed. We count only three objects in our Y_{105}-dropout sample that have their red circles making contact with a bright neighbor (SD05, SD15 and SD52). In fact, one of these three objects, SD05, is also selected by Bunker et al. (2009) as a candidate (see Table 2).

To better address whether our J_{125}-dropouts are preferentially close to foreground neighbors, we performed the following test. We generated 6 239 random positions in the field, and computed the distances between these positions and the centroids of the nearest objects in the H_{160}-based catalogs. Similarly, we also calculated the distances between the J_{125}-dropouts and the centroids
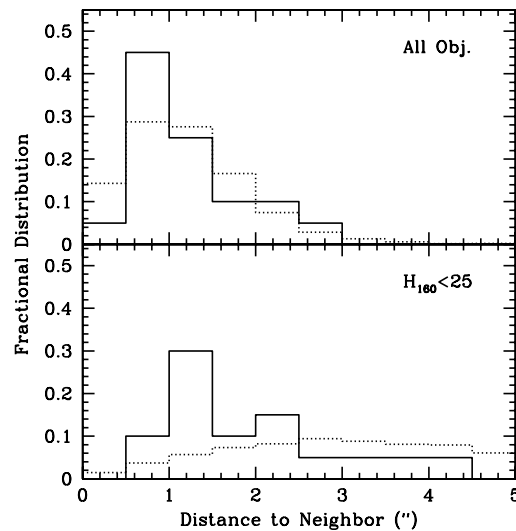
Fig. 15 Distribution of distances of the J_{125}-dropouts from the centroids of their nearest neighbors (*black* histograms) as compared with the same distribution calculated based on 6 239 random sightlines (*dotted* histograms). Both histograms are normalized using the respective total counts. The top panel uses all objects from the entire H_{160}-based catalog, while the bottom panel only uses the objects with $H_{160} < 25.0$ mag for statistical analysis.

of their nearest neighbors. The distributions of these distances are normalized by the total counts (6 239 and 20, respectively), and then compared as shown in Figure 15. The top panel shows the distributions when all the detected objects are used to select the nearest neighbors, while the bottom panel shows the result when only the objects with $H_{160} \leq 25.0$ mag are used. The bottom panel indicates that a fraction of our J_{125}-dropouts are indeed close to bright, foreground neighbors within $1.5''$, however, this fraction is only $\sim 40\%$ (red histogram), or eight objects in total. The six objects that we visually identified above are members of this population, and the other two objects are C047 and C067; both are at the border line of being $\sim 1.5''$ from their neighbors. From the distribution of the random positions (black histogram), the possibility of chance superposition within the same distance is 10.8% (which is much larger than the probability of 0.8% that Bouwens et al. estimated), and therefore the excess fraction of being close to bright foreground neighbors is no more than $\sim 30\%$.

We should point out that their proximity to foreground neighbors does not necessarily disqualify these dropouts from being legitimate candidates at high redshifts, because distance to a neighbor is never part of the LBG selection criterion. It is not likely that they are caused by noise fluctuations, because the "negative image" test does not show that the "negative dropouts" are preferentially produced in the regions close to bright objects. To strengthen this argument, we may examine similar cases in the Y_{105}-dropout sample where the candidates also have close foreground neighbors. These Y_{105}-dropouts are all detected in two bands in the rest of the sample, which does not lend support to the suggestion that they are spurious. It is also not likely that they are caused by defects in the detector or instrument optics, as such problems would happen to all the three bands and would affect all dropout samples, but no similar cases are seen in the z_{850}-dropout sample. Finally, it is also unlikely that these objects are physically associated with the neighbors, since none of the galactic stellar systems that we know would have such colors.

A possible explanation of these J_{125}-dropouts, which have close foreground neighbors, is that they are genuine galaxies at $z \approx 10$ which are gravitationally lensed by their foreground neighbors. The possibility that a significant fraction of galaxies at $z \approx 10$ being gravitationally lensed by foreground galaxies has been suggested before (e.g., Barkana & Loeb 2000). An order-of-magnitude estimate shows that our suggested $z \approx 10$ LF (see Sect. 6.3), which is still in the exponential part of the Schechter function till 29.4 mag and thus is extremely steep, is broadly consistent with this interpretation and could explain the observed rate of close neighbors because of the magnification bias. Assuming that the lens galaxies are singular isothermal spheres (SIS) and that their number density does not evolve, the lensing probability (before accounting for the magnification bias) at $z = 10$ is on the order of a few per cent (see Kochanek et al. 2004, eqs. [109] and [110]). At a separation of $\lesssim 1.5''$ from the foreground galaxies, the typical magnification factor is $\mu \lesssim 2$. The surface density of $z \approx 10$ galaxies at 29.00–29.75 mag (i.e., a factor of two lower than the detection threshold of 29.0 mag) as predicted by our LF is 58 arcmin^{-2}, which means that ~ 10–11 objects could be magnified to above our detection threshold if the lensing probability is $\sim 4\%$. Taking the survey incompleteness into account (see Sect. 6.3), we would expect 6–8 lensed J_{125}-dropouts in the WFC3 field, which would be in good agreement with the observed surface density. A detailed lensing analysis is beyond the scope of this work, and will be presented in a separate paper (Wyithe et al. in prep.). The possibility of lensing was dismissed by Bouwens et al. on the grounds that there were no highly magnified cases. Their argument again is flawed, because the probability of $\mu > 2$ is much lower at such separations, and a high magnification could only be obtained at a much closer distance to the center of the lens and thus a highly magnified image would not be detected anyway owing to the blending with the lens itself.

As we will show in the next section, including or excluding the J_{125}-dropouts that have close foreground neighbors actually does not statistically change any of our conclusions significantly.

6 INTERPRETATION AND DISCUSSION

Our analysis has resulted in 20 z_{850}-dropouts, 15 Y_{105}-dropouts, and 20 J_{125}-dropouts. While most of our z_{850}-dropouts are the same as those presented by other groups, most of our Y_{105}-dropouts and all of our J_{125}-dropouts are new discoveries. As detailed in Section 5, these new discoveries are the result of a more complete search in our reduced data at the faint levels. Our search is limited to $\lesssim 29.2$ mag, the limit that every group has independently adopted. A small number of candidates reported by other groups are missing from our samples, and such objects are either outside of our selection field or are at the borderline of the selection criteria and thus can be explained by our selection function. In the rest of this section, we discuss the implications of our results.

6.1 Photometric Redshifts of z_{850}-dropouts

The dropout selection can only roughly constrain the redshift distribution of the selected sources by providing a plausible yet rather wide redshift range on the order of $\Delta z \sim 1$. With the deep multi-band photometry of the red side of the Lyman-break, it is now feasible to further constrain the redshifts of the z_{850}-dropouts in our sample by using the SED fitting technique to derive their photometric redshifts ($z_{\rm ph}$). Since the vast majority of these sources is much fainter than the limit that can be reached by the spectroscopic capability of any current instruments, photometric redshifts will remain as the only redshift estimates that can be used for further applications in the near future. We only carried out these exercises for the z_{850}-dropouts but not for the Y_{105}-dropouts, as the latter only have useful photometric information in three bands.

Here we used the SED fitting code developed by HY to derive $z_{\rm ph}$. The population synthesis models of Bruzual & Charlot (2003; hereafter BC03) were used to simulate the fitting templates. We adopted a Simple Stellar Population (SSP; i.e., an instantaneous burst) and also a series of star

formation histories (SFH) of exponentially declining star formation rates with the time scale τ spanning from 10 Myr to 13 Gyr. The ages (T) of these models range from 1 Myr to 1 Gyr. The initial mass function (IMF) of Salpeter (Salpeter 1955) was used, with the cut-offs at 0.1 and 100 $M_\odot$. As we only have a limited number of passbands, we assumed solar metallicity and zero reddening to reduce the number of free parameters. These assumptions are justified by the study of Yan et al. (2005), where it is shown that the properties of galaxies at $z \approx 6$ are consistent with solar metallicity and very little dust. The restframe model spectra were redshifted to $z = 5.6$–12.0 with a step size of $\Delta z = 0.1$, and attenuated by the H I absorption along the line-of-sight using the formalism of Madau (1995). The resulting spectra were then convolved with the system response curves of the ACS and the WFC3 IR passbands to generate the model templates for fitting.

The SEDs of the z_{850}-dropouts were constructed from the Y_{105}-based catalog. We added 0.05 mag to the reported photometric errors in the catalog to account for the fact that the current WFC3 IR zeropoints are accurate to $\sim 5\%$ level. For the z_{850}-dropouts, their fluxes in $B_{435}V_{660}i_{775}$ were set to zero and thus did not contribute to the fitting. Any non-detections in the z_{850}-band were replaced with the 2-σ upper limits measured in the RMS map at the source locations within an $r = 0.2''$ aperture, and a fixed error of 0.1 mag was assigned to z_{850} in this case.

The fittings to the model templates were done in the flux domain using the standard least-squares-fit algorithm, with a self-consistency constraint that a galaxy should not be older than the age of the universe at the fit redshift. Four free parameters were involved in this process, namely, $z_{\rm ph}$, T, τ, and stellar mass (M_*). The best-fit values of these parameters are listed in Table 4 for these objects.

Because the WFC3 IR data still only sample the restframe UV wavelengths of these objects, they cannot break the severe degeneracy between these parameters. For this reason, the best-fit values listed here, especially those for T, τ and M_*, should only be taken as a general guideline rather than accurate measurements. The estimate of $z_{\rm ph}$ suffers less from the model degeneracy, as it mostly depends on estimating the location of the Lyman-break, which to first order is determined by the line-of-sight H I absorption rather than the intrinsic properties of galaxies. Figure 16 shows the histogram of $z_{\rm ph}$ distributions, which is centered at $z \approx 6.9$–7.0 as expected. We point out that the brightest z_{850}-dropout, which YW04b discovered using the NIC3 data, zdrop-A032, has $z_{\rm ph} = 6.9$. This is also consistent with the reported $z_{\rm ph} = 7.0$ in McLure et al. (2010).
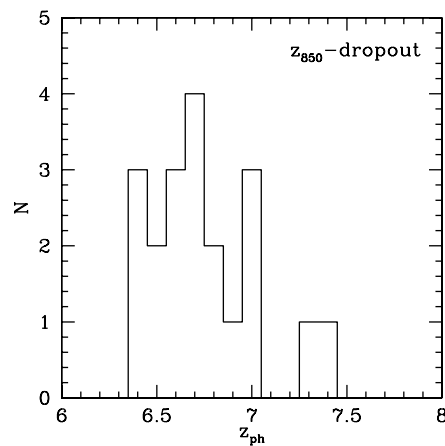

Fig. 16 Photometry redshift distribution of the z_{850}-dropouts, derived using SED fitting. This distribution is close to the expectation from the color selection criteria.

Table 4 Best-fit Model Parameters for $z \approx 7$ Sample[a]

ID	χ^2	$z_{\rm ph}$	$\mathcal{M}_*/M_\odot$	T (Myr)	τ (Gyr)
zdrop-A032	0.05	6.9	1.2×10^9	100	0.5
zdrop-A025	0.38	7.3	1.7×10^9	90	0.03
zdrop-A008	0.19	7.4	1.2×10^8	10	7.0
zdrop-A060	3.17	7.0	2.0×10^8	30	0.01
zdrop-A017	0.84	7.0	3.5×10^7	10	4.5
zdrop-A016	0.88	6.6	2.6×10^7	10	13.0
zdrop-A033	4.19	6.7	1.8×10^7	1	3.5
zdrop-A014	0.54	6.7	1.9×10^9	100	SSP
zdrop-A040	0.38	6.6	2.0×10^7	1	3.5
zdrop-A044	1.35	6.8	4.8×10^9	300	0.06
zdrop-A003	2.56	7.0	2.9×10^7	1	13.0
zdrop-A047	0.84	6.7	1.2×10^7	1	0.02
zdrop-A057	0.10	6.4	8.0×10^6	1	0.08
zdrop-A046	4.59	6.8	2.4×10^7	10	0.8
zdrop-A053	0.08	6.7	4.9×10^7	40	2.0
zdrop-A056	5.22	6.5	9.7×10^6	1	7.0
zdrop-A052	1.74	6.5	1.0×10^7	1	0.9
zdrop-A055	0.48	6.6	1.2×10^7	1	0.07
zdrop-A062	1.17	6.4	8.1×10^6	1	8.0
zdrop-A065	0.59	6.4	8.2×10^6	1	1.5

[a] Fitting templates derived using BC03 models, Salpeter IMF, solar metallicity, and zero reddening.

6.2 Stellar Masses of Galaxies at $z \approx 7$ and Beyond

Except for two previously studied sources, no other objects in our three dropout samples show a convincing case of detection in the deep GOODS IRAC images. These two sources are the two brightest z_{850}-dropouts, zdrop-A032 and A025. In the IRAC images, their locations are unfortunately very close to other unrelated objects nearby, and the extraction of their fluxes in IRAC passbands is non-trivial. Nevertheless, their stellar masses have been derived by Labbé et al. (2006), using the deblended IRAC photometry as the major constraint on their SEDs in the rest-frame optical. Depending on the models used, they derived stellar masses of a few $\times 10^9 M_\odot$ at $z_{\rm ph} \approx 6.8$ and 7.3 for zdrop-A032 (their ID 1147) and A025 (their ID 963), respectively. Interestingly, these values are not inconsistent with the best-fit values that we have obtained (see Table 4) using only the rest-frame UV flux measurements. There are a couple of more cases in Table 4 where the inferred stellar masses are at $\sim 10^9 M_\odot$ level, but none of them are significantly higher. This is in contrast to the i_{775}-dropout sample in the HUDF, where three $z \approx 6$ objects are significantly detected in IRAC 3.6 and 4.5 μm images and have stellar masses on the order of a few $\times 10^{10} M_\odot$ (Yan et al. 2005; Eyles et al. 2005).

As an effort to further constrain the average stellar mass of galaxies at $z \approx 7$ and beyond, we stacked these objects in both IRAC 3.6 μm and 4.5 μm channels. Sources that are not obviously blended with foreground objects (A032 and A025 are deemed to be blended) were selected, and their images in IRAC 3.6 μm and 4.5 μm were median-combined separately in the usual way. Objects that are close pairs were considered single objects (as they would not be separable by IRAC) and were only counted once. We first did this exercise for all three samples separately, and then also did the same for the merged z_{850}- and Y_{105}-dropout sample. We did not see any detection in any of these cases. Since no positive signal was detected, and the number of stacked objects is still limited, we are not able to derive any constraint stronger than a general statement that the majority of galaxies at $z \approx 7$ and beyond have stellar mass upper limits on the order of $10^9 M_\odot$.

Encouraged by the agreement between our results and those of Labbé et al.'s for zdrop-A032 and A025, we added up the stellar masses listed in Table 4 to derive the global stellar mass density at $z \approx 7$. This crude estimate gives $5.3 \times 10^5 \, M_\odot \, \mathrm{Mpc}^{-3}$, which is a factor of 10–12 smaller than that at $z \approx 6$.

6.3 Constraint on LF of Galaxies at Very High Redshifts

Our large dropout sample has offered a new opportunity to constrain the LF of galaxies at $z \approx 7$–10. Figure 17 shows our data points in red, derived based on the dropouts listed in Tables 1, 2 and 3, with error bars representing the Poisson noise. Three candidates that are formally (though only slightly) fainter than 29.0 mag (i.e., Ydrop-SD24, Jdrop-C056 and Jdrop-C034) are excluded from the statistics. For ease of connection to observations, the data are presented in the form of cumulative surface density per arcmin^2 as a function of apparent magnitude in a bin size of $\Delta m = 0.5$ mag, i.e., $N(\leq 26.5, 27.0, 27.5, 28.0, 28.5, 29.0)$, plotted at the center of each magnitude bin, i.e, at $m = (26.25, 26.75, 27.25, 27.75, 28.25, 28.75)$ mag. To be conservative, we also consider the possibility that our samples could be significantly contaminated at $z \approx 8$ and 10. In case of Y_{105}-dropouts, the green symbol in the 28.75 mag bin represents the surface density after excluding the objects that do not strictly satisfy $Y_{105} - J_{125} \geq 0.8$ mag if using the 2σ Y_{105}-band limits, which are all at $J_{125} \geq 28.5$ mag (see Table 2 and Sect. 5.2). In case of J_{125}-dropouts, the green symbols represent the results after excluding the objects that have close neighbors (see Sect. 5.4) and after taking into account the possible contamination due to noise fluctuations (see Sect. 5.3). These green symbols are slightly offset in magnitude for clarity. The cumulative surface densities predicted by various LFs are also shown for comparison. In all cases we use the non-evolving LF of YW04b at ≈ 6 as the fiducial one (hereafter YW04z6LF), which has the Schechter function parameters of $M^* = -21.03$ mag, $\Phi^* = 4.6 \times 10^{-4} \, \mathrm{Mpc}^{-3}$, and $\alpha = -1.8$.

The data points presented here have all been corrected for the survey incompleteness. We determine the incompleteness correction following the method used in YW04. For each dropout, a 15×15 pixel image stamp centered at its location in the discovery band was cut out and then randomly distributed to ~ 100 positions in the discovery image. For the z_{850}-dropouts, this was done in the Y_{105}-band mosaic. For the J_{125}-based and the JH-based Y_{105}-dropouts, this was done in the J_{125}-band mosaic and the JH-mosaic, respectively. For the J_{125}-dropouts, this was done in the H_{160}-band mosaic. The sections of the science images at these random locations were replaced by their image cutouts, but the RMS maps were not altered. This approach was used to simulate objects with the same properties (such as the brightness and the morphology) as the dropout under study and to apply different noise backgrounds to them (i.e., corresponding to different locations in the RMS maps). SExtractor was run on these new images following the same procedures as in Section 4, and we applied the same S/N≥ 3 thresholds to recover the simulated "dropouts." The average rate of recovery was taken as the completeness. For the z_{850}-dropout sample, it is complete in the $Y_{105} = 27.25$ mag bin and brighter; the incompleteness correction is a factor of 1.3, 1.3, 2.0 for the differential counts in the 27.75, 28.25 and 28.75 mag bins, respectively. For the Y_{105}-dropout sample, the incompleteness correction is a factor of 1.3 and 1.6 in the $J_{125} = 28.25$ and 28.75 mag bins, respectively. For the J_{125}-dropout sample, the correction is a factor of 1.5 and 1.7 in the $H_{160} = 28.25$ and 28.75 mag bins, respectively.

At $6.4 \lesssim z \lesssim 7.7$ (top left in Fig. 17), our data agree quite well with the LF estimate of B08 at $z \approx 7$ (hereafter B08z7LF) and the new estimates of Ouchi et al. (2009; Ou09z7), Oesch et al. (2010; Oe09z7) and McLure et al. (2010; M09z7) at $m \geq 27.5$ mag. The agreement at $m \leq 27.0$ mag with any LF, however, is not satisfactory. The data points in these two magnitude bins are the result of one single detection at the bright end, namely zdrop-A032. Therefore, the discrepancy could possibly be due to the combined effect of a small number statistics and "cosmic variance." Indeed, the spatial distribution of these dropouts shows apparent clustering, as indicated in the schematic plot at the
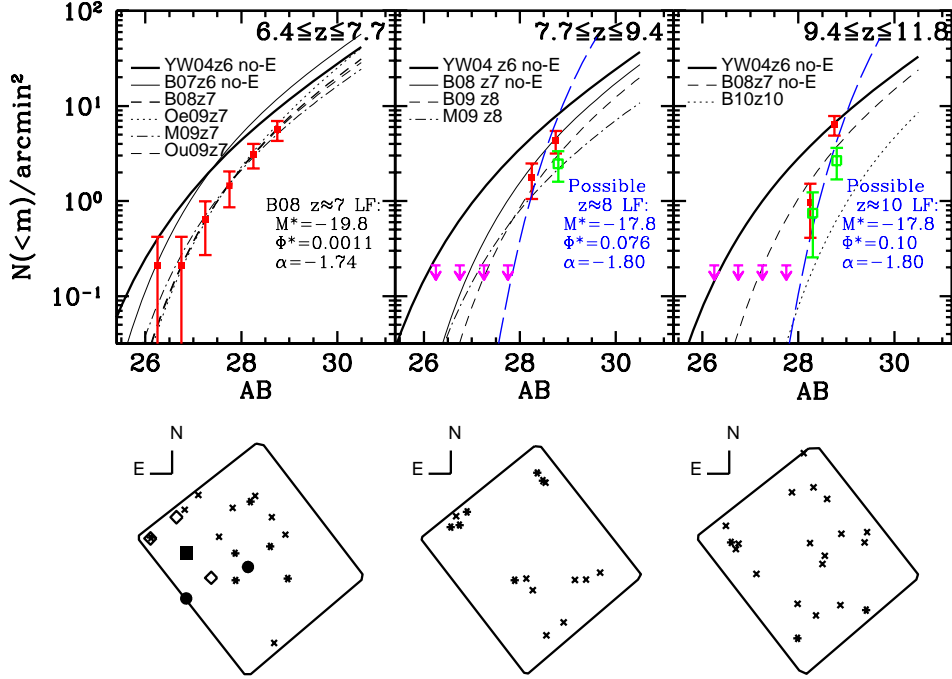
Fig. 17 (*Top*) Cumulative surface densities of the dropouts, compared to the predictions of various LF estimates. The data points have all been corrected for the survey incompleteness, and the error bars indicate 1σ Poisson noise. The green point in the middle panel includes only the Y_{105}-dropouts that satisfy $Y_{105} - J_{125} \geq 0.8$ mag when using the 2σ limits in the J_{125}-band. The green points in the right panel have excluded the J_{125}-dropouts that might be affected by the gravitational lensing of their foreground neighbors, and have taken the possible contamination due to the noise fluctuation into account. At $6.4 \leq z \leq 7.7$, the observations agree with various $z \approx 7$ LF estimates. At $7.7 \leq z \leq 9.4$ and $9.4 \leq z \leq 11.8$, the observations show a striking feature that there is no dropout at $m \leq 28.0$ mag. In both cases, the firm non-detections at $m \leq 28.0$ mag (purple upper limits) and the firm detections above it (especially in the $28.0 < m \leq 28.5$ mag bin) suggest that the underlying LF must be steeply rising towards lower luminosity. The steepness is consistent with the exponential part of the Schechter function, and we suggest possible LFs accordingly. Our tentative LFs are shown as the dashed blue curves. In particular, the LF at the $z \approx 10$ case is estimated *after* excluding the close-neighbor cases in the J_{125}-dropout sample (*bottom*). One potential source of uncertainty that can affect our interpretation is the effect of spatial clustering. While currently we are not able to derive useful constraints from the data, we show the spatial locations of the dropouts in these schematic figures (one for each sample), and point out that some apparent clustering signature does appear to be present. The symbols are coded according to their magnitudes: filled square — $m \leq 26.5$, filled circle — $27.0 < m \leq 27.5$, diamond — $27.5 < m \leq 28.0$, stars — $28.0 < m \leq 28.5$, cross — $28.5 < m \leq 29.0$. We do not have any candidates at $26.5 \leq m < 27.0$ at any of these redshifts.

bottom right panel of Figure 17. A wider survey is necessary to properly address the bright-end behavior.

At $7.5 \lesssim z \lesssim 9.4$ (top middle in Fig. 17), our data show a striking feature that there is no Y_{105}-dropout at $J_{125} \leq 28.0$ mag. This is noted in Bouwens et al. (2010) as well here; we see it at higher significance with our larger sample. Given the large uncertainty in the current measurement, especially at the faintest level (see the red and the green symbols), both of the LFs suggested by Bouwens et al. (2009) and McLure et al. (2010) are consistent with our data points. However, neither of them seem to be consistent with the upper limits at $J_{125} \leq 28.0$ mag: those LFs would predict 2–3 objects at this brightness level, where the current data are essentially complete (see Fig. 3). To satisfy both the data points and the upper limits, it seems that the underlying LF must be steeply rising towards faint luminosity. If the LF still takes the form of the Schechter function, the current data, while having reached ~ 29 mag ($M \sim -18.3$ mag), should still be sampling the exponential part of the LF. Motivated by this argument, we propose a possible LF that has the following Schechter function parameters:

$$M^* = -17.8 \,\mathrm{mag}, \qquad \alpha = -1.8, \qquad \Phi^* = 0.076 \,\mathrm{Mpc}^{-3}.$$

The cumulative surface density predicted by this LF, shown as the blue curve in the figure, is consistent with *both* the data points (red points) *and* the upper limits. Taking it at face value, this LF implies a dimming of 2.3 mag in M^* and a striking increase by a factor of $\sim 17\times$ in Φ^* as compared to the LF at $z \approx 7$.

It also seems that we could draw a similar conclusion from the LF at $9.4 \leq z \leq 11.8$ (top right in Fig. 17). The inferred cumulative surface density from our J_{125}-dropout sample is characterized by the non-detection at $H_{160} \leq 28.0$ mag and the steep increase in the last two bins, and we propose the following Schechter parameters, tuned to better fit the green symbols (i.e., excluding the objects with close foreground neighbors and taking into account the possible contamination due to noise fluctuations): $M^* = -17.8$ mag, $\alpha = -1.8$, $\Phi^* = 0.10 \,\mathrm{Mpc}^{-3}$. The predicted cumulative surface density from this LF is shown as the blue curve in the figure. Note that Φ^* increases by a factor of ~ 90 as compared to the LF at $z \approx 7$.

For convenience, we list the LF parameters from this study together with those of other LFs in Table 5. Again, a direct comparison of those seems to suggest a sudden change in the behavior of the galaxy LF at $z \approx 8$. While our proposed LFs at $z \approx 8$ and 10 are not yet demanded by the current observations, they are *allowed* by the data, and they seem to fit better than other alternatives.

Table 5 Schechter Function Parameters of Various LFs Discussed

LF Source[a]	M^* (mag)	Φ^* (Mpc^{-3} mag^{-1})	α
YW04z6LF, $z \approx 6$	-21.03	4.6×10^{-4}	-1.80
B07z6LF, $z \approx 6$	-20.24	1.4×10^{-3}	-1.74
B08z7LF, $z \approx 7$	-19.80	1.1×10^{-3}	-1.74
Ou09z7LF, $z \approx 7$	-19.90	1.1×10^{-3}	-1.70
Oe09z7LF, $z \approx 7$	-19.80	1.1×10^{-3}	-1.86
M09z7LF, $z \approx 7$	-20.11	7.0×10^{-4}	-1.72
this work, $z \approx 8$	-17.80	7.6×10^{-2}	-1.80
this work, $z \approx 10$	-17.80	1.0×10^{-1}	-1.80

[a] Ref: YW04z6LF – Yan & Windhorst (2004b); B07z6LF – Bouwens et al. (2007); B08z7LF – Bouwens et al. (2008); Ou09z7LF – Ouchi et al. (2009); Oe09z7LF – Oesch et al. (2010); M09z7LF – McLure et al. (2010)
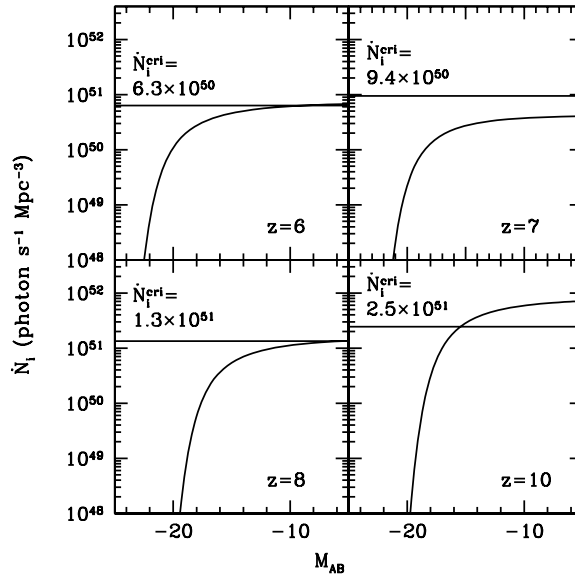
Fig. 18 Ionizing photon production rate density from galaxies ($\dot{N}_i$; the curves) compared to the critical value ($\dot{N}_i^{\mathrm{cri}}$; the horizontal lines) that is required to keep the universe completely ionized at various redshifts. As presented in YW04a, galaxies can account for the entire ionizing photon budget at $z \approx 6$ if their LF has a steep faint-end slope α. Assuming galaxies have similar intrinsic properties, the calculated $\dot{N}_i$ at $z \approx 7$ using B08z7LF (which has a steep α) could be $\sim$40%–50% of $\dot{N}_i^{\mathrm{cri}}$, which might be desirable because one would expect the neutral fraction of hydrogen at $z \approx 7$ is still $\gg 0$. If we apply the LFs that we tentatively propose for $z \approx 8$ and 10 (see Table 5), the implied $\dot{N}_i$ would cross over $\dot{N}_i^{\mathrm{cri}}$ if the LFs do not cut-off and the reionization would be completed too early.

6.4 Implications for Cosmic Hydrogen Reionization

Since $z \approx 8$–10 extends well *into* the cosmic reionization epoch, and our LFs sample an area in the parameter space that has not yet been explored, here we discuss their implication for reionization.

A question that has been intensively studied is whether the star-forming galaxy population can be the source of cosmic hydrogen reionization, or at least be an important part of it. To answer this question, one can calculate the integrated production rate density of photons at $\lambda < 912$ Å from galaxies ($\dot{N}_i$), and then compare to the critical ionizing photon emission rate density ($\dot{N}_i^{\mathrm{cri}}$) that is necessary to balance the combination rate. Madau et al. (1999; MHR) have given a recipe (their eqn.[26]) to calculate $\dot{N}_i^{\mathrm{cri}}$ at arbitrary redshifts, with the only free parameter being the hydrogen clumping factor (C). Calculating $\dot{N}_i$ is done by integrating the LF and then multiplying by a factor that describes the product of the number of Lyman photons produced per unit galaxy (which in principle can be inferred from the UV slope of typical LBGs) and the fraction of those that can escape the galaxy (f_{esc}). Another approach is to compare to the critical SFR density ($\dot{\rho}_*^{\mathrm{cri}}$) that is derived from $\dot{N}_i^{\mathrm{cri}}$ using a galaxy population synthesis model (given in MHR eqn.[27]). To do this, one needs to know the SFR of a typical galaxy, and this is almost always done by using the conversion between L_{UV} and SFR as given in Madau et al. (1998; their eq.[2]).

A full discussion of the application of these two approaches is beyond the scope of this paper; here we only point out that (1) currently the results from these two methods do not necessarily agree,

(2) comparing to $\dot{\rho}_*^{\mathrm{cri}}$ implicitly assumes a particular population synthesis model and the particular IMF that this model takes, and (3) comparing to $\dot{N}_i^{\mathrm{cri}}$ only depends on the choice of the SED shape at $\lambda < 912$ Å but does not depend on any model.

YW04a studied this problem at $z \approx 6$ using this first approach, and proposed a steep LF faint-end slope of $\alpha < -1.6$ in order to bring $\dot{N}_i$ in agreement with $\dot{N}_i^{\mathrm{cri}}$. YW04b soon confirmed that $\alpha \lesssim -1.8$ using the HUDF data, and pointed out that star-forming galaxies alone could have contributed to most of the reionizing photon background. Since then, the very steep LF faint-end slope at $z \approx 6$ has been confirmed by other studies (e.g., Bouwens et al. 2006; B07), and it has been widely accepted that star-forming galaxies, especially those at the faint-end, must have played an important role in the reionization. YW04a adopted $f_\nu \propto \nu^{-1.8}$ at $\lambda < 912$ Å, which would allow the YW04z6LF to produce $\dot{N}_i = \dot{N}_i^{\mathrm{cri}}$ at $z = 6$ if integrating the LF to $M = -15.7$ mag and assuming $f_{\mathrm{esc}} = 0.12$ and $C = 30$. Both f_{esc} and C are highly uncertain. While the recent simulation of Pawlik et al. (2009) suggests a much lower clumping factor of $C = 6$, the studies of f_{esc} seem to point to a small value of $f_{\mathrm{esc}} \lesssim 0.02$–$0.05$ (e.g., Siana et al. 2007; but see also Shapley et al. 2006). The combination of the two would still make $\dot{N}_i$ be in agreement with $\dot{N}_i^{\mathrm{cri}}$, only with the crossover now being at $M = -9.0$ mag. Adopting B07z6LF would give a similar answer, with the only difference being that this LF only needs to be integrated to $M = -13.3$ mag to have the crossover.

Here we consider how our new results could shed light on the source of the reionization problem in the following context. Assuming that the SED power law index adopted by YW04a is appropriate such that the galaxy population alone can indeed sustain the ionizing background at $z \approx 6$, would the galaxies at $z \approx 7$–10 produce the right amount of ionizing photons if these galaxies have the same properties as those at $z \approx 6$? Simply speaking, now we hope that $\dot{N}_i \lesssim \dot{N}_i^{\mathrm{cri}}$, because we do want a large number of ionizing photons such that the reionization can happen, and at the same time we do not want too many ionizing photons such that the reionization would have ended too early and there would be no neutral hydrogen left to create the Gunn-Peterson troughs that have been observed at $z \approx 6.5$. YW04a has investigated this problem and pointed out that one solution is to have the Schechter LF break down at some certain minimum luminosities to prevent this from happening. As we now have hints that the galaxy LF at $z \approx 8$ and beyond might imply an unexpectedly large number of faint galaxies, it is prudent to investigate this problem further.

Our results are summarized in Figure 18, assuming $C = 6$ and $f_{\mathrm{esc}} = 0.02$. For simplicity, we quote $\dot{N}_i$ in units of 10^{51} photons s^{-1} Mpc^{-3}. At $z = 6$, $\dot{N}_i$ is calculated using YW04z6LF, and it crosses $\dot{N}_i^{\mathrm{cri}}$ at around $M = -9.0$ mag as mentioned before. At $z = 7$, $\dot{N}_i$ is calculated using B08z7LF, which is consistent with the new observations as discussed in the previous section. In this case, $\dot{N}_i$ asymptotically approaches 0.42, which is about a factor of $2.2\times$ less than $\dot{N}_i^{\mathrm{cri}}$. This might be somewhat too low, but it does satisfy the requirement that the ionizing photons are not overproduced. At $z = 8$, $\dot{N}_i$ calculated using the LF parameters quoted in Table 5 does not cross over $\dot{N}_i^{\mathrm{cri}}$ until $M = -6.7$ mag. It is not clear if the Schechter function still holds at such lower luminosity levels; if it does, in order *not* to reionize the universe completely at $z = 8$, it seems that the contribution of ionizing photons from objects at $M > -6.7$ mag should be cut-off, for example, by invoking $f_{\mathrm{esc}} = 0$ for these galaxies. One way to achieve the cut-off is to completely shut down the star formation. Since very low mass halos are not capable of cooling down to a sufficiently low temperature to form stars, such a cut-off might not be surprising. At $z = 10$, the cross-over happens at a much brighter level of $M = -15.4$ mag, and similar reasoning suggests that $f_{\mathrm{esc}} = 0$ is required for galaxies fainter than this threshold. This would mean that most of the ionizing photons at these stages are from a number of the brightest objects, and this does seem to be consistent with a sudden on-set of reionization. Of course, the above numbers should only be taken as a guide, because we do not yet have any definite knowledge about C and f_{esc}, nor do we know the LF very well. Nevertheless, this very simple exercise could potentially be very useful.

6.5 Global Star Formation Rate Density and Stellar Mass Density

If we adopt the conversion between $L_{\rm UV}$ and SFR as $L_{\rm UV} = 8.0 \times 10^{27} \times$ SFR (MPD eq.[2]) for the Salpeter IMF, we can easily calculate the global SFR density (GSFRD; $\dot{\rho}_*$) at $z \gtrsim 7$. The results are shown in the top panel of Figure 19 for $z \approx 7$, 8 and 10, together with the GSFRD at $z \approx 6$ for comparison. We do not include the correction for dust extinction at these four redshifts, as it is not well constrained at the moment. To see the overall evolution trend, the GSFRD at lower redshifts (Hopkins & Beacom 2006) are also shown.

In Figure 19, the red squares at $z = 6.0$ and 7.0 are obtained by integrating the LFs in the luminosity regimes that have been directly probed by the existing observations. While the LFs derived by various groups are different, they all agree with the direct observations down to the survey limits. Therefore, by only integrating to the survey limits, one can take the derived values as the lower bounds of the GSFRD. Specifically, the one at $z = 6.0$ is obtained by integrating YW04z6LF to 30.0 mag, which is the limit of the i_{775}-dropout search in the ACS HUDF. Similarly, the one at $z = 7.0$ is derived by integrating B08z7LF to 29.0 mag, which is the limit of the z_{850}-dropout search in the current WFC3 HUDF. These values are $\dot{\rho}_* = (12.33, 5.50) \times 10^{-3} \, M_\odot \, {\rm yr}^{-1} \, {\rm Mpc}^{-3}$ at $z = (6.0, 7.0)$, respectively.

The red squares at $z = 8.6$ and 10.6 are obtained by adding the contribution from the observed dropouts after applying proper corrections for the survey incompleteness. In other words, they correspond to the red symbols in Figure 17. These values are $\dot{\rho}_* = (2.54, 3.77) \times 10^{-3} \, M_\odot \, {\rm yr}^{-1} \, {\rm Mpc}^{-3}$ at $z = (8.6, 10.6)$, respectively.

As the observations at $z \approx 8$ and 10 still have large uncertainties, it is useful to consider the lower limits of the GSFRD at these redshifts. These are shown in Figure 19 as the thick solid line that outlines the bottom of the grey region. The lower limit at $z \approx 8$ is obtained by including only the most robust Y_{105}-dropouts that satisfy $Y_{105} - J_{125} \geq 0.8$ mag when using the $2\,\sigma$ upper limit in J_{125} (i.e., the objects in the first part of Table 2), and is calculated using the $1\,\sigma$ lower limit (due to Poisson noise) of the surface density thus derived. The lower limit at $z \approx 10$, on the other hand, is obtained by statistically subtracting the contribution from the possible contamination from the noise fluctuation, and is also calculated using the $1\,\sigma$ lower limit of the surface density thus inferred. Specifically, these values are $\dot{\rho}_* = (0.82, 1.42) \times 10^{-3} \, M_\odot \, {\rm yr}^{-1} \, {\rm Mpc}^{-3}$ at $z = (8.6, 10.6)$, respectively.

We should also consider how high the GSFRD could possibly be. This would require us to extrapolate the LFs and then integrate, and it is somewhat uncertain in the sense that the limit to which the extrapolation (and hence the integration) should stop is arbitrary. For the sake of the argument, here we choose to stop at $M = -15.0$ mag, or $0.01 \times L^*(z = 3)$. At $z \approx 10$, this limit corresponds to $m \sim 32.7$, which would be difficult to reach even with the JWST. The results of this exercise are $\dot{\rho}_* = (0.019, 0.011, 0.022, 0.116) \, M_\odot \, {\rm yr}^{-1} \, {\rm Mpc}^{-3}$ at $z = (6.0, 7.0, 8.6, 10.6)$, respectively. The values at $z = 6.0$ and 7.0 are based on YW04z6LF and B08z7LF, respectively, while the values at $z = 8.6$ and 10.6 are based on the LFs that we propose in Section 6.3. These values are shown as the upper envelope of the grey region in Figure 19. If a fainter integration limit is adopted, this upper envelope will be higher. For comparison, the orange dotted line shows the GSFRD calculated based on the $z \approx 8$ and 10 LFs of Bouwens et al. (2009, 2010), integrated to the same limit of $M = -15.0$ mag.

This grey region reflects the uncertainties in the current GSFRD measurement at $z \gtrsim 7$. The major source of uncertainty is in the LF estimates at $z \gtrsim 8$, which is not likely to be improved until significantly deeper and wider data are available. Nevertheless, it is worth pointing out that if our proposed LFs at $z \approx 8$ and 10 are correct, the evolution of the GSFRD could be very different from what one would extrapolate from the trend seen at lower redshifts. As the upper envelope of the grey area implies, the GSFRD could start at an early time at a very high value, decline to a valley at $z \approx 7$, and then increase again towards $z \approx 6$. While the suggestion of this trend is still only tentative, such a behavior of the GSFRD in the early time seems to fit naturally into the picture of the reionization.
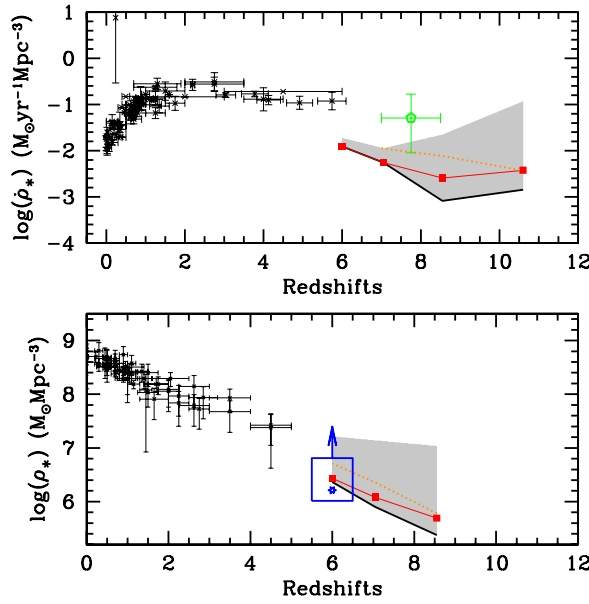
Fig. 19 (*Top*) Evolution of the global SFR density (GSFRD; $\dot{\rho}_*$) from $z \approx 10$. The values at $z < 6$ are taken from Hopkins & Beacom (2006). The grey region reflects the uncertainty in the current estimates at $z \gtrsim 6$. The red squares at $z = 6.0$ and 7.0 are obtained by integrating YW04z6LF and B08z7LF to the dropout search limit of $m = 30.0$ (for $z \approx 6$) and 29.0 mag (for $z \approx 7$), respectively. The red squares at $z = 8.6$ and 10.6 are derived by adding the contribution from our Y_{105}- and J_{125}-dropouts, respectively, and the proper correction for incompleteness. The bottom boundary of this region (indicated by the thick black line) shows the GSFRD derived based on the conservative estimates of the dropout number densities at $z \approx 8$ and 10 (but still having the incompleteness correction applied). For $z \approx 8$, this estimate only takes into account the Y_{105}-dropouts that satisfy $Y_{105} - J_{125} \geq 0.8$ mag when using the $2\,\sigma$ limits in Y_{105}, and is calculated using the $1\,\sigma$ lower limit (due to Poisson noise) of the Y_{105}-dropout surface density thus inferred. For $z \approx 10$, this estimate is obtained by statistically subtracting the possible contamination due to the noise fluctuation, and is also calculated using the $1\,\sigma$ lower limit of the surface density thus inferred. The top boundary of the grey region is obtained by integrating the LFs to the fiducial limit of $M = -15$ mag. For $z = 6.0$ and 7.0, YW04z6LF and B08z7LF are used, respectively. For $z = 8.6$ and 10.6, our proposed LFs at $z \approx 8$ and 10 are used, respectively. The orange dotted line represents the results by integrating the LFs at $z \approx 7$, 8 and 10 of Bouwens et al. (2007, 2009, 2010) to $M = -15$ mag. The green symbol is the GSFRD at $z \approx 8$ as derived in Kistler et al. (2009) based on GRB 090423 at $z \approx 8.1$ (*bottom*). Evolution of the global stellar mass density (GSMD; ρ_*) from $z \approx 10$. The values at $z < 6$ are taken from Wilkins et al. (2008). The grey region here maps the grey region in the top panel (including the symbols), and is obtained by integrating the GSFRD over time (assuming zero stellar mass density at $z = 10$). The blue star at $z = 6.0$ and the surrounding box, taken from Yan et al. (2006), represent the GSMD estimate at this redshift and the associated uncertainty, which should be taken as a strict lower limit because only detected galaxies were used. It is likely that the vast majority of the stellar masses assembled over the reionization epoch is still undetected at $z \approx 6$.

A very high GSFRD in the early universe has also been suggested by Kistler et al. (2009) based on Gamma-Ray Bursts (GRBs) at high redshifts, in particular GRB 090423 at $z \approx 8.1$ (Salvaterra et al. 2009; Tanvir et al. 2009). The green pentagon in the upper panel of Figure 19 shows the GSFRD at $z \approx 8$ as derived in Kistler et al. (2009). If our LF at $z \approx 8$ is integrated to $M \approx -8.5$ mag, the inferred GSFRD will match that of Kister et al. Using the LF of Bouwens et al. (2010) or McLure et al. (2010), however, the inferred GSFRD will be a factor of five too low even when integrating to zero luminosity.

From the GSFRD, we can obtain the *expected* global stellar mass densities (GSMD; ρ_*) by a straightforward integration over time. Assuming that the universe started from zero stellar mass at $z \approx 10$, the GSMD thus calculated are shown as the grey region in the bottom panel of Figure 19, which maps the grey GSFRD region in the top panel. The lower boundary corresponds to $\rho_* = (0.23, 0.08, 0.02) \times 10^7 \, M_\odot \, \mathrm{Mpc}^{-3}$ at $z = (6.0, 7.0, 8.6)$, respectively, the red squares correspond to $\rho_* = (0.27, 0.12, 0.05) \times 10^7 \, M_\odot \, \mathrm{Mpc}^{-3}$ at $z \approx (6.0, 7.0, 8.6)$, respectively, and the upper envelope corresponds to $(1.63, 1.37, 1.08) \times 10^7 \, M_\odot \, \mathrm{Mpc}^{-3}$ at $z \approx (6.0, 7.0, 8.6)$, respectively. For comparison, the orange dotted line here maps the orange dotted line in the top panel. Note that the upper envelope of the GSMD at $z \approx 6$ is significantly higher than what has actually been detected by *Spitzer* IRAC observations (Yan et al. 2006; blue symbols). This is not necessarily a discrepancy, because the latter is a lower limit. However, it does suggest that the vast majority of the stellar masses assembled during the reionization epoch have yet to be detected at $z \approx 6$. Future observations with the JWST will be able to determine whether this is the case.

7 SUMMARY

In this work, we have searched for galaxy candidates at $z \approx 7$ to 10 using the deepest ever near-IR observations obtained by the new WFC3 instrument that was recently installed on the *HST*. While these existing data are only from the first epoch of observations of the entire program, they have allowed us to explore the universe at the highest redshifts ever possible.

By carefully reducing and analyzing these precious data, we are able to take full advantage of the unprecedented depth that these new observations can offer. Using the standard Lyman-break selection technique, we have found 20 z_{850}-dropouts, 15 Y_{105}-dropouts and 20 J_{125}-dropouts, which are highly probable (S/N> 3) candidate Lyman-break galaxies in three wide redshift ranges at $z \approx 7$, 8 and 10, respectively. These are the largest samples of very high-redshift galaxies to date. Among them, four z_{850}-dropouts and ten Y_{105}-dropouts have not been reported by others, and the objects in the entire J_{125}-dropout sample are new discoveries. We have derived photometric redshifts for the z_{850}-dropouts by fitting their multi-band SEDs, and the distribution of these photometric redshifts gives us an extra level of confidence that our dropout selection indeed selects galaxies at high redshifts. While the J_{125}-dropouts are single-band detections and hence are less secure as compared to the z_{850}- and Y_{105}-dropouts, our test indicates that at least $> 50\%$ of them are very likely genuine candidates at $z \approx 10$. We point out that the recent criticism that the majority of our J_{125}-dropouts are implausibly too close to "bright foreground" objects is not justified. While there are a few cases where our dropouts are close to a neighbor, the excess fraction is $\sim 30\%$. While they could be due to some contaminants of unknown origins, we suggest that these objects could be genuine $z \approx 10$ galaxies that are gravitationally lensed by their foreground neighbors, and that the seemingly high rate could be explained by their intrinsically very steep LF and the magnification bias. Future observations with the JWST will be able to prove or refute this interpretation. We stress that including or excluding them from the sample does not change our major conclusions.

Our search for dropouts does not go beyond the limit that has been reached by other independent studies. While the number density of z_{850}-dropouts agrees more or less with the expectations based on the previous works, the most surprising fact is that there are no bright candidates in the Y_{105}- *and* J_{125}-dropout sample. The firm detections and the firm non-detections above and below ~ 28.0 mag

in *both cases* seem to suggest a very steep increase in the surface density. While the current data are not yet able to set stringent constraints because of the small number statistics and the limited dynamic range in luminosity, we find that the sharp increase could be explained by the exponential part of the Schechter function. Motivated by this, we propose a rather unusual set of Schechter function parameters to describe the LFs at $z \approx 8$ and 10. As compared to their counterpart LF at $z \approx 7$, our proposed LFs at $z \approx 8$–10 have M^* fainter by ~ 2.0 mag and Φ^* higher by a factor of 17–90. We caution that these LFs are still tentative and are not yet demanded by the data. Nevertheless, they are allowed by the existing observations and agree with the available data better than other alternatives. If these LFs still hold at a level beyond our current detection limits, they would imply that there is a sudden emergence of an extremely large number of low-luminosity (by our local standard) galaxies when we look back in time to $z \approx 10$, and their persistence extends well into $z \approx 8$. While this is totally unexpected, it is fully consistent with, and naturally fits in the picture of the cosmic hydrogen reionization, which is believed to begin at $z \approx 11$ and end at $z \approx 6$. Such galaxies could account for the entire ionizing photon budget at the reionization epoch; in fact, it is likely that they would overproduce ionizing photons and therefore either the escape fraction of Lyman photons must be extremely low in galaxies that are below some certain luminosity threshold, or galaxies below such threshold were not formed at all.

Based on our dropout samples, we have derived the global SFR densities at $z \approx 7$–10. The exact value of $\dot{\rho}_*$ depends on the exact form of the LFs and also the limit down to which the integration of the Schechter function is still valid. As the answers to both questions will remain highly uncertain until the JWST is launched, we derive our results based on a range of possibilities that cover the most conservative estimate to the most radical one. If our proposed LFs at $z \approx 8$ and 10 are indeed valid, they imply an extremely high global SFR density ($\dot{\rho}_*$) in the early universe. Using $M = -15.0$ mag ($L = 0.01 \times L^*(z = 3)$) as the fiducial limit, the integration of our LFs shows that $\dot{\rho}_*$ could start from $\sim 0.12 \ M_\odot \ \mathrm{yr}^{-1} \ \mathrm{Mpc}^{-3}$ at $z \approx 10$, rapidly decline to $\sim 0.01 \ M_\odot \ \mathrm{yr}^{-1} \ \mathrm{Mpc}^{-3}$ at $z \approx 7$, and then start to rise again towards lower redshifts. A very high GSFRD at $z \gtrsim 8$ is in line with the picture of the reionization, and has also been suggested based on the study of long-duration GRBs. While the universe might have started vigorously forming stars at $z \approx 10$ and seems to have turned $\sim 1.4 \times 10^7 \ M_\odot \ \mathrm{Mpc}^{-3}$ worth of matter into stars over the ~ 300 Myr to $z \approx 7$, the most massive galaxies at $z \approx 7$ are still only on the order of a few $\times 10^9 \ M_\odot$. A large fraction of stellar masses assembled during the reionization epoch seems undetected so far at $z \approx 6$. The dramatic decrease of Φ^* from $z \approx 10$ to 7 probably suggests that big galaxies at $z \approx 7$–6 have gained their masses mostly through the merging of subsystems. We have detected a few cases of close pairs and mergers indicative of such a scenario, however, the statistics is still too limited to draw any meaningful constraint. This work, together with those of other groups, shows that it will be essential for the JWST to fully explore the $z \gtrsim 8$ regime.

References

Barkana, R., & Loeb, A. 2000, ApJ, 53(1), 613

Beckwith, S. V., Stiavelli, M., Koekemoer, A. M., et al. 2006, AJ, 132, 1729

Bertin, E., & Arnouts, S. 1996, A&AS, 117, 393

Bouwens, R. J., et al. 2003, ApJ, 595, 589

Bouwens, R. J., et al. 2004, ApJ, 606, L25

Bouwens, R. J., et al. 2006, ApJ, 653, 53

Bouwens, R. J., et al. 2007, ApJ, 670, 928 (B07)

Bouwens, R. J., et al. 2008, ApJ, 686, 230

Bouwens, R. J., et al. 2010, ApJ, 709, L133

Bouwens, R. J., et al. 2009, arXiv:0912.4263

Bouwens, R. J., Illingworth, G. D., Thompson, R. I., Franx, M. 2005, ApJ, 624, L5

Bradley, L. D., et al. 2008, ApJ, 678, 647

Bruzual, G., & Charlot, S. 2003, MNRAS, 344, 1000

Bunker, A., Wilkins, S., Ellis, R., et al. 2009, MNRAS, submitted (arXiv:0909.2255)

Bunker, A. J., Stanway, E. R., Ellis, R. S., & McMahon, R. G. 2004, MNRAS, 355, 374

Capak, P., et al. 2009, arXiv0910.0444

Coe, D., et al. 2006, AJ, 132, 926

Chary, R.-R., et al. 2007, ApJ, 665, 257

Dickinson, M., Stern, D., Giavalisco, M., et al. 2004, ApJ, 600, L99

Dickinson, M., et al. 2000, ApJ, 531, 624

Eyles, L., Bunker, A., et al. 2005, MNRAS, 364, 443

Eyles, L., et al. 2007, MNRAS, 374, 910

Fan, X., et al. 2002, AJ, 123, 1247

Fan, X., et al. 2006, AJ, 132, 117

Fruchter, A., & Hook, R. N. 1997, SPIE, 3164, 120

Fruchter, A., & Hook, R. N. 2002, PASP, 114, 144

Giavalisco, M., et al. 2004a, ApJ, 600, L93

Giavalisco, M., et al. 2004b, ApJ, 600, L103

Gunn, J. E., & Peterson, B. A. 1965, ApJ, 142, 1633

Hickey, S., Bunker, A., Jarvis, M. J., Chiu, K., & Bonfield, D. 2010, MNRAS, 404, 212

Hopkins, A. M., & Beacom, J. F. 2006, ApJ, 651, 142

Iye, M., et al. 2006, Nature, 443, 186

Kimble, R. A., MacKenty, J. W., O'Connell, R. W., & Townsend, J. A. 2008, in Space Telescopes and
    Instrumentation 2008: Optical, Infrared, and Millimeter, eds. Oschmann, de Graauw, MacEwen, and Howard
    A., Proceedings of the SPIE, Volume 7010, pp. 70101E-70101E-12 (2008)

Kistler, M. D., Yuksel, H., Beacom, J. F., Hopkins, A. M., & Wyithe, J. S. B. 2009, ApJ, 705, L104

Kneib, J.-P., Ellis, R. S., Santos, M. R., & Richard, J. 2004, ApJ, 607, 697

Kochanek, C. S., Schneider, P., & Wambsganss, J. 2004, Gravitational Lensing: Strong, Weak & Micro,
    Proceedings of the 33rd Saas-Fee Advanced Course, eds., G. Meylan, P. Jetzer, & P. North (Berlin: Springer-
    Verlag)

Koekemoer, A. M., Fruchter, A. S., Hook, R. N., & Hack, W. 2002, in The 2002 HST Calibration Workshop:
    Hubble after the Installation of the ACS and the NICMOS Cooling System, eds. Santiago Arribas, Anton
    Koekemoer, & Brad Whitmore, Baltimore, USA, 337

Komatsu, E., et al. 2010, ApJS, submitted (arXiv:1001.4538)

Labbé, I., Bouwens, R., Illingworth, G. D., et al. 2006, ApJ, 649, L67

Madau, P. 1995, ApJ, 441, 18

Madau, P., Haardt, F., & Rees, M. J. 1999, ApJ, 514, 648 (MHR)

Madau, P., Pozzetti, L., & Dickinson, M. 1998, ApJ, 498, 106 (MPD)

Mobasher, B., et al. 2005, ApJ, 635, 832

McLure, R. J., Dunlop, J. S., Cirasuolo, M., et al. 2010, MNRAS, 403, 960

Oesch, P. A., Stiavelli, M., Carollo, C. M., et al. 2007, ApJ, 671, 1212

Oesch, P. A., Bouwens, R. J., Illingworth, G. D., et al. 2010, ApJ, 709, L16

Ouchi, M., et al. 2009, ApJ, 706, 1136

Pawlik, A., Schaye, J., & van Scherpenzeel, E. 2009, MNRAS, 394, 1812

Richard, J., et al. 2008, ApJ, 685, 705

Salpeter, E. E. 1955, ApJ, 121, 161

Salvaterra, R., et al. 2009, Nature, 461, 1258

Siana, B., et al. 2007, ApJ, 668, 62

Shapley, A., Steidel, C. C., Pettini, M., Adelberger, K. L., & Erb, D. 2006, ApJ, 651, 688

Sobral, E., et al. 2009, MNRAS, 398, L68

Stanway, E. R., Bunker, A. J., & McMahon, R. G. 2003, MNRAS, 342, 439

Stanway, E. R., Bremer, M. N., Squitieri, V., Douglas, L. S., & Lehnert, M. D. 2008, MNRAS, 386, 370

Stark, D. P., et al. 2007, ApJ, 663, 10

Tanvir, N. R., et al. 2009, Nature, 461, 1254

Thompson, R. I., Illingworth, G., Bouwens, R., et al. 2005, AJ, 130, 1

Wilkins, S. M., Trentham, N., & Hopkins, A. M. 2008, MNRAS, 385, 687

Willis, J. P., Courbin, F., Kneib, J.-P., & Minniti, D. 2008, MNRAS, 384, 1039

Yan, H., & Windhorst, R. 2004a, ApJ, 600, L1 (YW04a)

Yan, H., & Windhorst, R. 2004b, ApJ, 612, L93 (YW04b)

Yan, H., Dickinson, M., Eisenhardt, P., et al. 2004, ApJ, 616, 63

Yan, H., Dickinson, M., Stern, D., et al. 2005, ApJ, 634, 109

Yan, H., Dickinson, M., Giavalisco, M., et al. 2006, ApJ, 651, 24

Zheng, W., et al. 2009, ApJ, 697, 1907